

Effects of injector geometry on acoustically coupled flame dynamics

Arin Hayrapetyan, Andres Vargas and A.R. Karagozian o

¹Department of Mechanical and Aerospace Engineering, UCLA, Los Angeles, CA, USA Corresponding author: A.R. Karagozian, ark@ucla.edu

(Received 10 May 2025; revised 13 August 2025; accepted 30 August 2025)

The present experiments investigated the combustion dynamics of single and coaxial laminar diffusion flames within a closed cylindrical acoustic waveguide, focusing on their response to acoustic forcing at a pressure antinode. Nine alternative fuel injectors were used to examine the effect of injector jet diameter and configuration, tube wall thickness, annular-to-inner area and velocity ratio, and jet Reynolds number (below 100) on flame behaviour under different applied frequencies and pressure perturbation amplitudes. Fundamental flame-acoustic coupling phenomena were identified, all of which involved symmetric flame perturbations. These included sustained oscillatory combustion (SOC), multi-frequency periodic liftoff and reattachment (PLOR), permanent flame lift-off (PFLO) with low-level oscillations, and flame blowoff (BO). The phase lag between acoustic forcing and flame response was quantified, providing valuable insights into the coupling dynamics and transition behaviours. Findings revealed how various geometrical and flow characteristics could affect flame stability and resistance to blowoff, even under similar acoustic forcing conditions. Analysis of high-speed spatiotemporal visible imaging using proper orthogonal decomposition (POD) uncovered additional distinct phase portraits and spectral signatures associated with instability transitions, which, coupled with specific dynamical characteristics, enabled new insights into the relevance of injector geometrical characteristics and flow conditions in addressing acoustically coupled combustion instabilities.

Key words: combustion, flames, laminar reacting flows

1. Introduction

Combustion instabilities have long posed challenges in aerospace propulsion systems due to their potentially catastrophic effects, and they remain challenging to fully understand, quantify and control (Harrje 1972; Candel 1992; Lieuwen *et al.* 2001; Culick &

Kuentzmann 2006). These instabilities arise from the coupling between self-sustained acoustic oscillations in chamber pressure and local flow velocity creating periodic heat release, leading to amplified oscillations when in phase. Augmentation of such oscillations is a critical concern in the development of liquid rocket engines and gas turbine combustors, particularly in systems using hydrocarbon-fuelled combustion (Crocco & Cheng 1956), which is of increasingly widespread use in the U.S. Understanding and quantifying this coupling dynamic is essential for predicting and controlling such instabilities.

The present experiments significantly expand upon prior studies of acoustically coupled combustion in the vicinity of a pressure node (PN). These prior studies include combustion of neat fuel droplets (Sevilla-Esparza et al. 2014; Bennewitz et al. 2018), liquid nanofuel mixtures (Sim et al. 2019, 2020a), and gaseous methane laminar microjets of various geometries and at jet Reynolds numbers below 100 (Sim et al. 2020b; Vargas et al. 2023, 2025), all subject to transverse forcing in the vicinity of a PN (or velocity antinode) associated with a standing acoustic wave. Near a PN, the bulk influence on a flame or hot/low density region is dominated by velocity perturbations in the transverse direction, in addition to a bulk acoustic radiation force acting on the lower-density region (Tanabe et al. 2000). In the vicinity of a PN, the acoustic radiation force results in a net deflection of the flame away from the pressure node (Tanabe et al. 2005), and these are observed in the aforementioned fuel droplet and gaseous fuel jet-based experiments at UCLA. In contrast, the present study investigated flame behaviour at a pressure antinode (PAN) associated with the standing acoustic wave, where transverse velocity perturbations are minimal near the flame and the bulk influence of the flame response would be driven by local pressure perturbations. Recent studies of jet flames in the vicinity of a PAN or PN for single and coaxial gaseous fuel jet configurations have been explored experimentally at the Air Force Research Laboratory (AFRL), with tests conducted at higher Reynolds numbers (up to 10 000) (Plascencia et al. 2024a,b). Despite the limitations in geometry and injector options, AFRL's results in the vicinity of a PN have shown comparable dynamics to those in the UCLA experiments (Vargas 2022; Vargas et al. 2023, 2025). This motivates further exploration of flame dynamics at or near a PAN in a more easily controllable combustion environment with a broad parameter space and the ability to study alternative injector geometries, which are among the goals of the present study. Specific observations from the PAN studies at AFRL (Plascencia et al. 2024a,b) will be described herein.

A number of studies have explored non-forced, low-Reynolds-number diffusion flames to enhance understanding of the stabilisation processes governing both attached and lifted flames. Unforced lifted buoyant flames at Reynolds numbers around 50 are found to naturally exhibit low-frequency oscillations of the order of a few Hz (Won *et al.* 2000). Chung & Lee (1991, 1997) investigate the characteristics of lifted flames, demonstrating that the flame base has a tribrachial (triple flame) structure. Their findings indicate that lifted flames become unstable when the fuel's Schmidt number is less than unity, with upstream mass diffusion playing a crucial role in flame behaviour. Linan, Vera & Sanchez (2015) investigate ignition, liftoff and extinction phenomena, emphasising the role of triple flames in flame stabilisation and propagation, highlighting the importance of the Damköhler number and flame stretch in determining flame behaviour. Gao *et al.* (2017) further demonstrated that heat recirculation through the burner wall can stabilise flames near extinction by minimising heat loss and extending the flammability limit, noting that burner thermal conductivity and wall thickness influence flame stability, with lower conductivity and thinner walls promoting excess-enthalpy combustion.

The influence of acoustic excitation on diffusion flames has been studied primarily for turbulent or transitional jets, typically focusing on the influence of external perturbations created within the fuel jet or injection system on flame stability, structure and combustion

dynamics. For example, Baillot & Demare (2002, 2007) perform longitudinal (axial) acoustic forcing on non-premixed methane lifted flames at jet Reynolds numbers in the range 3000-6000, and map different response regimes dependent on forcing frequency and axial vertical velocity fluctuations. These include regions in which a flapping flame that periodically attaches to the injector can exist, with the flame alternating between an attached or lifted state, or being in a permanently lifted state. Williams et al. (2007) explore the transient interactions between vortices and flames in axially forced, buoyant laminar methane-air coflow slot diffusion flames, identifying specific forcing conditions under which the generation of air-side vortices synchronise at exactly half the excitation frequency of the fuel stream. Experiments by Chen, Wang & Zhang (2012) involving a fuel jet excited axially within a longitudinally oriented acoustic waveguide with a square crosssection suggest that flame dynamics and fuel flow are highly sensitive to the phase angle and flame position within the acoustic field, with significant variations observed in velocity antinode regions, inducing complex flame structures and strong vorticity. Numerical simulations of acoustically coupled diffusion flames (Chen et al. 2017; Magina, Acharya & Lieuwen 2019) typically employ simplifications in the fluid mechanics as well as the reaction kinetics. Yet quantification of the flame transfer function, the normalised ratio of periodic combustion heat release and flow oscillations, reveals insights in frequency and amplitude dependence for flame response.

In earlier UCLA studies involving both burning droplets (Bennewitz et al. 2018; Sim et al. 2019, 2020a) and gas microjets (Sim et al. 2020b) in the vicinity of a PN, phaselocked OH* chemiluminescence imaging was used to evaluate the Rayleigh index, a key indicator of the degree of coupling between acoustic waves and unsteady heat release rate in flames. According to the Rayleigh criterion (Rayleigh 1896), thermoacoustic instabilities are enhanced when heat release rate fluctuations q' are in phase with local pressure fluctuations p', or nearly so. The Rayleigh index, a measure of the phase and magnitude of this coupling, is used to identify regions of stability and instability in acoustically forced flames. When the Rayleigh index G, shown in (1.1), is positive over the integrated period T, the heat release rate and pressure fluctuations are in phase, or close to being such, leading to energy transfer from the flame to the acoustic field and reinforcing thermoacoustic instabilities. When negative, the instability is said to be damped. Yet, both droplet and fuel jet combustion instability studies at UCLA involving excitation near a PN demonstrate that a transition in flame dynamics, either involving periodic partial extinction and reignition (Bennewitz et al. 2018) or periodic liftoff and reattachment (Sim et al. 2020a) can also produce a negative Rayleigh index, despite the fact that the instability is clearly not damped. Here, the heat release rate q' is shown to be directly related to the OH* chemiluminescence in the volume enveloping the flame structure. These observations have led to high-speed visible flame imaging and the application of proper orthogonal decomposition (POD) analysis of the imaging to explore characteristic signatures for flame dynamics, as will be discussed for the present studies.

$$G = \frac{1}{T} \int_0^T \int_V p'(x, t) q'(x, t) \, dV \, dt.$$
 (1.1)

As noted previously, the experiments conducted at AFRL involving transverse external acoustic excitation of jet diffusion flames are the closest in general configuration to the present studies. In an exploration of single and coaxial fuel jets at two different Reynolds numbers (4700 and 10 000) and with two different annular-to-inner jet velocity ratios for the coaxial configuration (Plascencia *et al.* 2024*a*), high-speed schlieren and OH* chemiluminescence imaging are used to explore flame—acoustic coupling at a pressure

antinode created via transverse excitation in a closed waveguide. Brouzet et al. (2022) demonstrate in large-eddy simulations of the AFRL experiments that the transverse acoustic modes do in fact induce strong longitudinal velocity perturbations, significantly affecting injector acoustics and causing fluctuations in mass flow rates. For PAN excitation at three different frequencies (360 Hz, 775 Hz and 1150 Hz), with increasing amplitudes of excitation, flame response is categorised as transitioning from being anchored to the injector, to being periodically lifted (then reattached) to the injector, then permanently lifted from the injector. The single-fuel jet demonstrates all three responses for different applied frequencies and amplitudes of excitation, with the ability of the flame to remain anchored at higher amplitude forcing when excitation occurs at a higher frequency rather than a lower frequency. In contrast, the coaxial fuel jet, with air injected in the annular region at very low annular-to-inner velocity ratios (0.02 and 0.05), shows an opposite trend: at the highest frequency excitation condition, the flame remains anchored only at relatively low amplitude excitation before transitioning to periodic lifting and permanent liftoff, while at lower frequencies, the flame is fully anchored for a range of excitation amplitudes. Subsequent experiments (Plascencia et al. 2024b) examining coaxial fuel jets exposed to a PAN for a range of annular-to-inner velocity ratios (R = 0–0.3) confirmed that, indeed, the flame appeared to be less stable when exposed to high-amplitude excitation at higher frequencies, with marginal benefits to flame stability for lower velocity ratios. For both sets of experiments, jet Reynolds number does not appear to have a very strong influence on flame dynamics, though higher Re values do appear to produce flames that can avoid the periodic liftoff condition altogether, transitioning immediately to permanent flame liftoff. While the higher excitation frequency is relatively close to the natural (unforced) flame instability frequency, approximately 1500 Hz (Plascencia 2021), the limited datasets in the tests make it difficult to explain many of these trends. This, in part, motivates the present study.

The present experimental work investigated the effects of alternative injector geometries and flow conditions on acoustically coupled combustion dynamics for laminar non-premixed gaseous methane microjets, with single and coaxial configurations. The jet flames were positioned at a PAN within a closed waveguide at atmospheric pressure, under transverse excitation. While the low-Reynolds-number regime explored here was considerably smaller than that explored in the acoustically coupled combustion experiments of Plascencia *et al.* (2024*a,b*), similar dynamics between the two studies near a PN suggest the potential insights that the present PAN studies can provide. For both single and coaxial jets under acoustic excitation, the flame response here exhibited distinct transitions with increasing forcing amplitude. As will be shown and discussed in detail, deeper insights into the coupling dynamics and transitional behaviours of acoustically driven flames reveal the key parameters that govern flame stability and resistance to blowoff.

2. Experimental set-up

The experimental set-up builds upon prior UCLA studies and is shown in figure 1. The cylindrical aluminium waveguide has an internal diameter of 11.4 cm and a length of 90 cm, with a burning microjet and optical access at the centre. Enclosed by a movable assembly of opposing 8 Ω loudspeakers, positioned 61 cm apart, a standing acoustic wave was generated inside the waveguide at atmospheric pressure with a prescribed frequency and amplitude. In the present configuration, the speakers were operated under an in-phase sinusoidal signal to produce a PAN, or equivalently, a velocity node, at the waveguide's geometric centre, where the flame was located. The forcing frequency f_a was systematically varied between 55 Hz and 185 Hz to explore its influence on

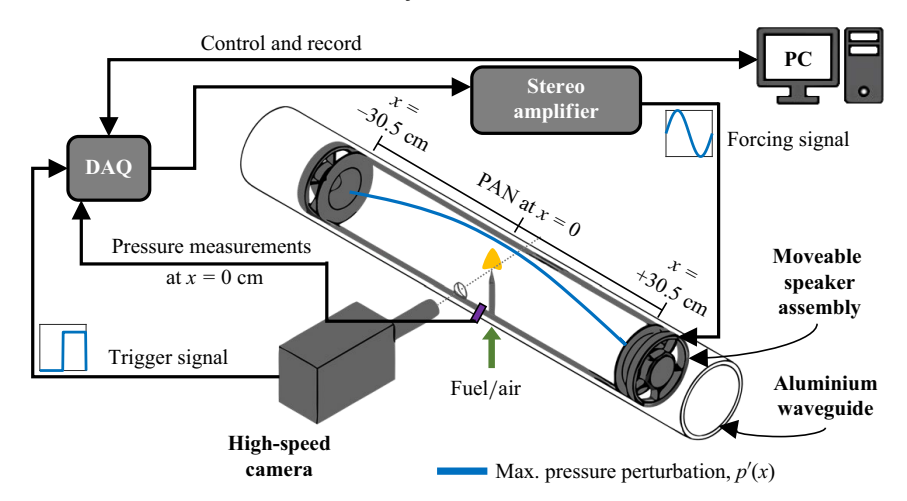


Figure 1. Experimental set-up of the gaseous jet inside the acoustic waveguide, with high-speed visible imaging and pressure transducer measurement at the flame location.

the combustion process. The natural oscillations of low-Reynolds-number jet flames are extremely weak and occur at very low frequencies, as noted previously (Won et al. 2000), and in the present experiments, were not detected. Consequently, the forcing frequencies explored were significantly higher than that of any natural instability. The degree of forcing in this study was quantified in terms of the local pressure perturbation p', where 100 samples per acoustic cycle were recorded via a Kulite XCS-093-5D miniature pressure transducer embedded in the waveguide wall at the flame location (geometric centre of the waveguide, x = 0). The maximum pressure perturbation p'_{max} was obtained by the time-interpolated estimate of the dominant frequency component's amplitude using a fast Fourier transform (FFT) of the signal. Earlier experiments by the group (Sevilla-Esparza et al. 2014; Bennewitz et al. 2018) demonstrate the compatibility of one-dimensional (1-D) acoustic analysis with the creation of a standing wave in a waveguide, where the analytical expression for the spatial variation in pressure perturbation p'(x) matches the experimental observed condition, as does its related velocity perturbation u'(x). Acoustic forcing at 140 Hz represented a resonant frequency corresponding to a quarter-wavelength mode of 61 cm, maximising the output p'_{max} for a given forcing voltage. A significant drop in output p'_{max} was observed for forcing frequencies beyond 140 Hz, and this limited the maximum frequency explored.

A high-speed visible monochrome camera (Photron Mini AX200) with a 200 mm macro lens was used to image the flame responses to the acoustic forcing, acquired with line-of-sight visible flame luminosity images at 1000 frames per second (FPS), with a corresponding shutter speed of 998 μ s. The images were captured with 12-bit depth and have a maximum possible intensity value of 4095. Experimental cases were conducted at a constant forcing frequency, where the forcing amplitude to the speakers increased in a staircase-like fashion. The camera was set to capture 341 frames before sending a trigger signal to a LabVIEW script via the DAQ to step up the forcing amplitude, controlled by a small increase in the voltage to the speakers. The voltage increase was set to observe a step in p'_{max} no greater than 8 Pa. A 1-second delay was set between steps to allow for abundant time for the speakers and standing wave to step up in amplitude. Since the waveguide lacked an exhaust for combustion products, data acquisition was conducted within a short time window (within 2 minutes) after flame ignition, followed by purging of

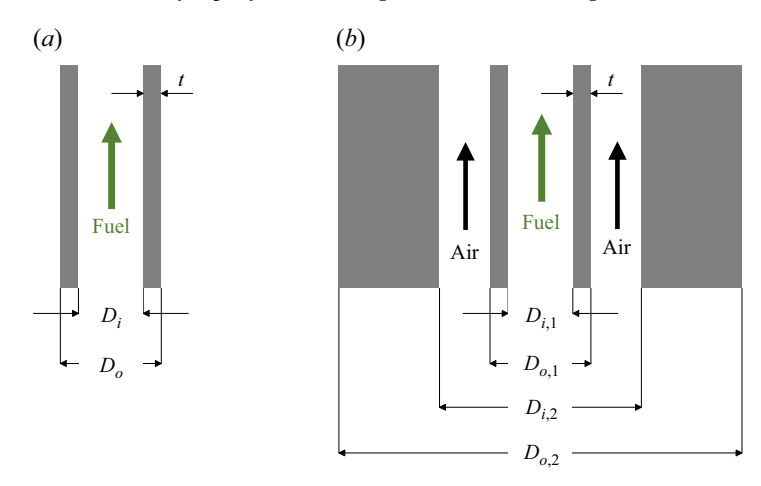


Figure 2. Injector configuration of the (a) single and (b) coaxial jet. The side view illustrates the important dimensions including inner and outer diameters (subscripts i and o, respectively) for both inner and outer tubes (subscripts 1 and 2, respectively), as well as the inner tube wall thickness t. Refer to table 1 for the corresponding dimensions for both single and coaxial configurations.

the waveguide with fresh air before the next test. The influence of the buildup of hot burnt gases in the waveguide on the flame (e.g. on p'_{max} corresponding to blowoff) occurred well beyond the data collection time window, typically after 3 minutes for a single-jet flame burning at the higher flowrate of fuel. The images were downloaded and preprocessed to improve the signal-to-noise ratio via an in-house denoising neural network (Hayrapetyan, Vargas & Karagozian 2025). The processed datasets were then analysed using POD to extract dynamic mode shapes and their temporal evolution.

The present experiments explored single methane and coaxial methane-air injectors to study the effects of different injector configurations on flame response to pressure antinode forcing. The single jets consisted of straight round stainless steel tubes from which gaseous methane emanated, whereas the coaxial jets consisted of concentric tubes in which gaseous methane emanated from the inner jet and air from the annular region, depicted in figure 2. Figure 2(a) illustrates the single-jet geometry, identifying the inner and outer diameters, D_i and D_o , and wall thickness t. Figure 2(b) illustrates the coaxial jet geometry, displaying the inner and outer diameters for the inner methane jet, $D_{i,1}$ and $D_{o,1}$, respectively, inner tube wall thickness t, and the inner and outer diameter for the annular air tube, $D_{i,2}$ and $D_{0,2}$. Four different single-jet and five different coaxial-jet geometries with varying flow configurations were tested to study the effect of fuel Reynolds number Re_1 , inner tube diameter and wall thickness, outer-to-inner velocity ratio R, and annular-to-inner area ratio AR. Table 1 lists the dimensions and area ratios of the various stainless steel single and coaxial configurations. The naming convention for the four single jets was tailored to the jet's characteristic inner diameter and wall thickness, similar to that described by Forliti et al. (2020). For example, the term Small-Thick injector refers to the single jet with a comparatively small inner diameter and relatively thick wall thickness, and the Large-Thin injector corresponds to the single jet with the comparatively large inner diameter and relatively thinner wall. Similarly, the coaxial jets were named to reflect their comparative area ratio and relative wall thickness, e.g. where the SAR-Thin coaxial jet corresponded to the comparatively small-area-ratio (SAR) coaxial jet with a relatively thin inner wall, while the XLAR-Thick coaxial jet corresponded to the comparatively extra-large-arearatio (XLAR) injector with a relatively thick inner wall. The lengths of the injectors

Single Jets	D_i (mm)	D_o (mm)	t/D_i	Coaxial Jets	AR	$t/D_{i,1}$	<i>D</i> _{<i>i</i>,1} (mm)	D _{0,1} (mm)	<i>D</i> _{<i>i</i>,2} (mm)	<i>D</i> _{0,2} (mm)
Small-Thin	0.46	0.79	0.37	SAR-Thin	7.3	0.28	1.02	1.59	3.18	6.35
Small-Thick	0.51	1.59	1.06	MAR-Thick	29.3	1.06	0.51	1.59	3.18	6.35
Medium-Thin	1.02	1.59	0.28	LAR-Thin	45.2	0.37	0.46	0.79	3.18	6.35
Large-Thin	1.59	3.18	0.50	LAR-Thick	45.0	1.06	0.51	1.59	3.76	5.56
-				XLAR-Thick	100.5	1.06	0.51	1.59	5.33	6.35

Table 1. Single- and coaxial-jet dimensions.

Single Jets	Re	$Q \pmod{\min^{-1}}$	$U_{jet} \ ({ m ms}^{-1})$
Small-Thin	15	5.5	0.56
	20	7.2	0.74
	40	14.3	1.46
Small-Thick	20	8.0	0.66
	40	16.1	1.32
Medium-Thin	11	8.9	0.19
	20	16.2	0.34
	46	35.9	0.76
Large-Thin	8	9.8	0.08
	20	25.1	0.21

Table 2. Alternative single jet flow conditions.

and upstream fuel/air delivery lines were selected to avoid resonant coupling with the forcing frequency range as determined through theoretical approximation of acoustic wave propagation in tubes as well as experimental verification.

3. Unforced flame behaviour

3.1. Single jets

A range of fuel Reynolds numbers was investigated across various single jets, with a key matching Reynolds number of 20 and a maximum value of 46. The Reynolds number at the jet exit was determined based on the mean bulk velocity over the cross-sectional area at a prescribed volumetric flow rate. The range of Reynolds numbers, corresponding fuel volume flow rates Q, and bulk fuel jet velocities U_{jet} explored for the single jets is given in table 2. The Small-Thin, Medium-Thin and Large-Thin jets, although having slightly different non-dimensional wall thicknesses (as listed in table 1), were studied to investigate the influence of inner diameter on flow and reactive processes in an acoustic environment. The Small-Thin and Small-Thick jets, despite having slightly different inner diameters, were included to demonstrate the general trends associated with variations in tube wall thickness. Figure 3 shows instantaneous visible-imaging snapshots of various unforced single jet flame geometries at a range of Reynolds numbers, acquired at 30 FPS. The images are scaled to match accurate proportions across the different injectors, with the axes non-dimensionalised by the jets' respective inner diameter. The definitions of the flame standoff distance δ_f and flame height δ_h are indicated in the figure.

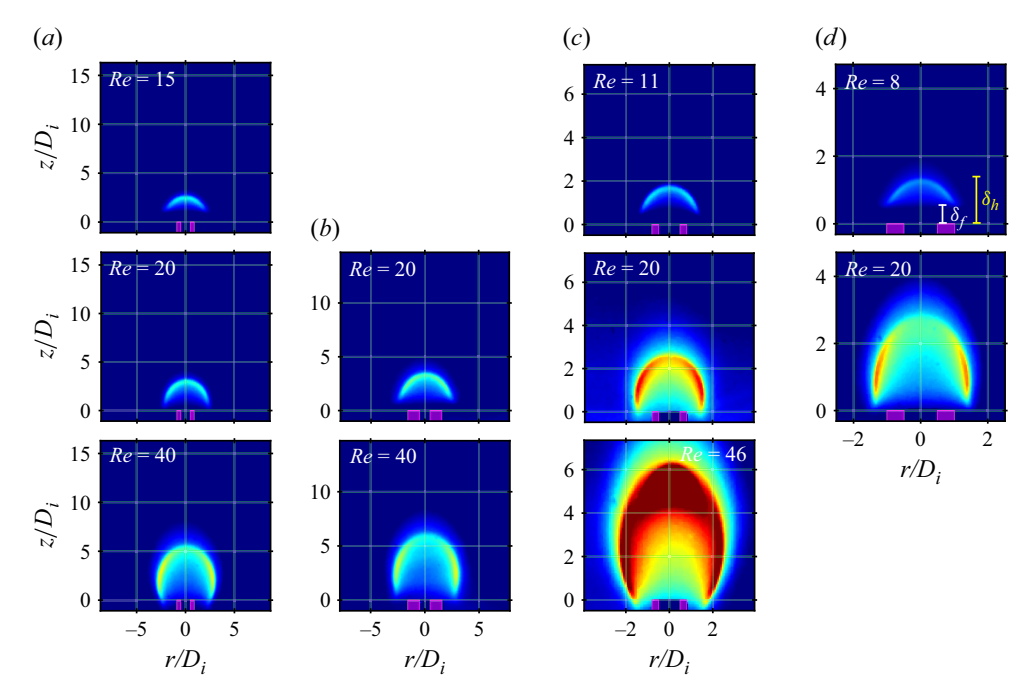


Figure 3. Instantaneous visible images of the unforced flame for the different single-jet geometries at the jet Reynolds number indicated, acquired at 30 FPS. (a) Small-Thin,(b) Small-Thick,(c) Medium-Thin and (d) Large-Thin.

At a matched Reynolds number of 20 (middle row of figure 3), the jet with the smallest inner diameter produced the smallest flame due to its lowest volumetric fuel flow rate, yet it exhibited the highest bulk jet velocity. In contrast, the jet with the largest diameter had the highest fuel flow rate but the lowest jet velocity. This difference in fuel flow rate impacted both the flame size and its luminosity or intensity, as seen by the comparative colourmap. In all cases, without acoustic forcing, the flame remained attached to the jet exit and burned steadily; a natural frequency or instability was not detected. The flame would burn with mostly unperturbed structure and intensity for several minutes before extinguishing due to the depletion of oxidiser in the enclosed waveguide. To maintain manageable flow conditions, the maximum fuel flow rate studied was under 36 ml min⁻¹. Higher Reynolds number jets required much larger forcing amplitudes to produce transition in flame dynamics, as will be discussed; such amplitudes could not be achieved with the present loudspeakers. Additionally, higher fuel flow rates were avoided to prevent soot buildup in the waveguide and to allow for a sufficient time window for data collection before any effects related to oxygen depletion occurred. As shown in figure 3 for the Medium-Thin injector at a Reynolds number of 46, brightly burning soot particles accumulated at the top of the flame and eventually recirculated through the waveguide, which appeared as high-illumination streaks in the imaging.

It is noted that in the absence of excitation, the range of Grashof numbers in the present experiments (single and coaxial configurations) encompassed approximately 20–800, which produced Richardson numbers in the range of 0.5–2.0, where $Ri \equiv Gr/Re^2$. Hence, in the absence of acoustic excitation, buoyancy and inertial forces were often comparable. This was consistent with our observation in figure 3, for example, that the unforced flame images generally were lifted slightly above the burner, but did not flicker or elongate,

Coaxial Jets	Re_1	Q_1 (ml min ⁻¹)	U_1 (m s ⁻¹)	R_{max}
SAR-Thin	10	8.1	0.17	2.40
	20	16.1	0.33	2.10
MAR-Thick	40	16.1	1.32	0.44
LAR-Thin	20	7.3	0.74	0.40
LAR-Thick	20	8.1	0.66	0.60
	40	16.1	1.32	0.38
XLAR-Thick	40	16.1	1.32	0.35

Table 3. Alternative coaxial jet flow conditions with maximum sustainable velocity ratio.

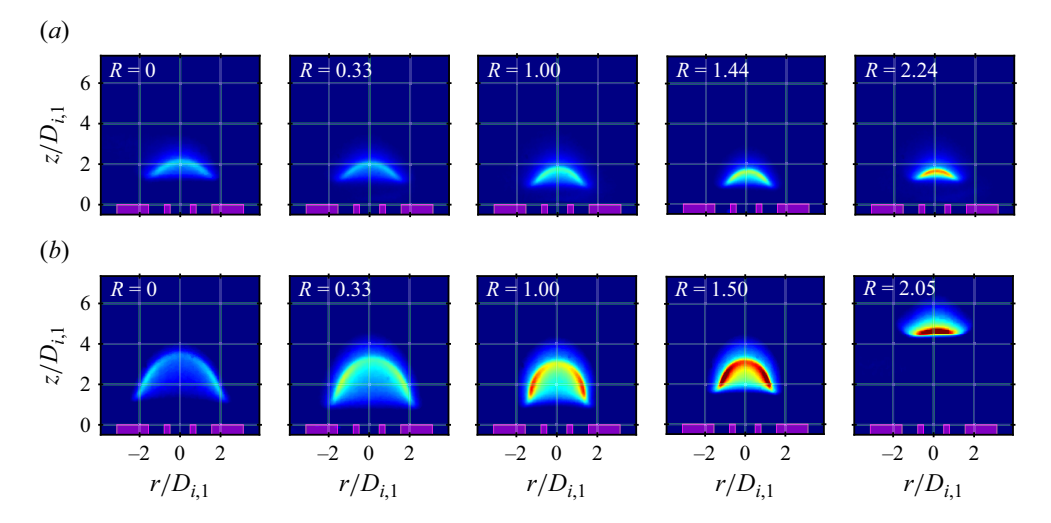


Figure 4. Instantaneous visible images of the unforced flame, acquired at 30 FPS, for the SAR-Thin coaxial jet at (a) $Re_1 = 10$ and (b) $Re_1 = 20$ for various velocity ratios.

having a compact and stable shape. The same was observed for coaxial fuel jets, described as follows.

3.2. Coaxial jets

The coaxial injector geometry enabled exploration of a much broader parameter space in the present experiments. A range of velocity ratios were studied between the various coaxial jets, where the fuel Reynolds numbers and velocity ratios were matched among the different configurations. Table 3 lists the coaxial jet flow conditions explored here, where the maximum R at which the flame can stabilise for these Reynolds numbers is listed as R_{max} . Figure 4 shows instantaneous images of the unforced flames emanating from the SAR-Thin coaxial jet at fuel Reynolds numbers of 10 and 20 for various velocity ratios, acquired at 30 FPS. Like the single jets, these flames could burn steadily for several minutes in the enclosed waveguide without changes to size, intensity or natural liftoff height, and no natural frequency or instability associated with the flame was detected. With varying velocity ratio, changes in flame intensity and the unforced liftoff height were observed. In acoustic-free conditions, methane flames (Schmidt number < 1) are known to blowoff beyond a given volume flow rate Q without lifting (Chung & Lee 1991). However, the present experiments revealed that the introduction of an annular air coflow

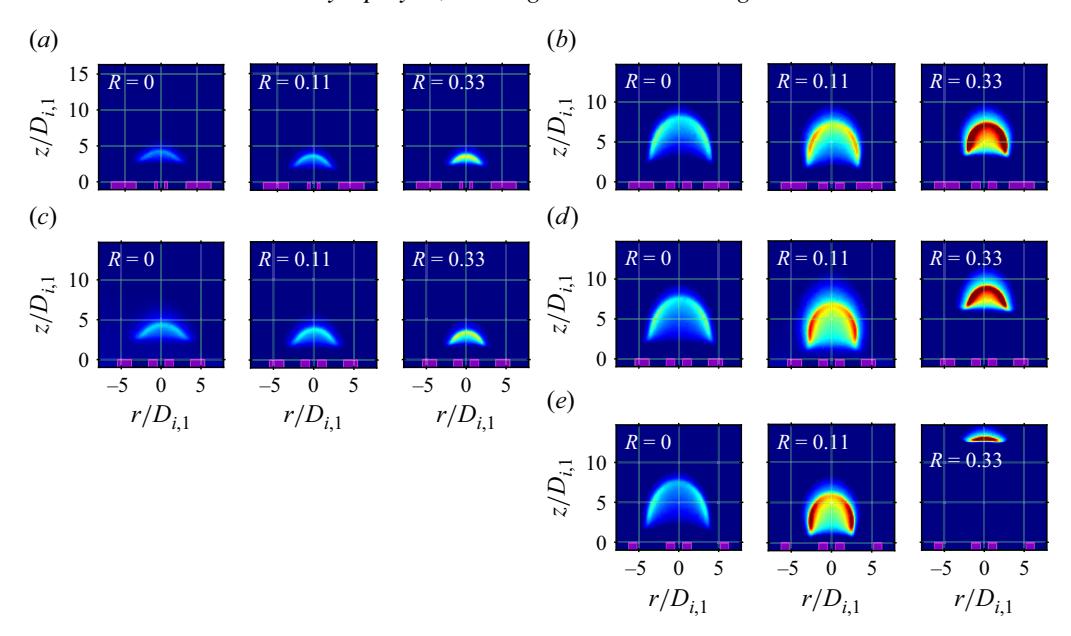


Figure 5. Instantaneous visible images of the unforced flame, acquired at 30 FPS, for various coaxial jet geometries at the prescribed Reynolds number and velocity ratio R. (a) LAR-Thin, $Re_1 = 20$, (b) MAR-Thick, $Re_1 = 40$, (c) LAR-Thick, $Re_1 = 20$, (d) LAR-Thick, $Re_1 = 40$ and (e) XLAR-Thick, $Re_1 = 40$.

in a coaxial jet configuration enabled sustained lifting of the flame at higher velocity ratios R, prior to blowoff. This effect could result from reduced strain rates and the formation of recirculation zones in the vicinity of the inner wall separating reactants, all of which can contribute to flame stabilisation (Habib & Whitelaw 1979; Feikema, Chen & Driscoll 1991). In the absence of coflow (R=0), the flame stabilised over (on top of) the coaxial configuration. With the introduction of air coflow, the flame became more bent and pinched, hovering a little closer to the fuel jet exit, reducing the standoff distance. However, as the velocity ratio increased beyond a certain threshold, the flame liftoff grew, resulting in a naturally lifted flame. This trend was consistent across all coaxial jets, though the specific velocity ratio at which liftoff occurred was unique to each fuel Reynolds number and coaxial jet geometry.

To investigate the effects of wall thickness on flame blowoff resistance, the LAR-Thin and LAR-Thick configurations, which featured matching area ratios and similar inner diameters but differed in inner tube wall thickness (by a factor of three), were compared, with unforced snapshots shown in figure 5. The unforced flames for both of these coaxial jets at a fuel Reynolds number of 20 for matched velocity ratios are shown in figures 5(a) and 5(c). The unforced flames emanating from these injectors with matched flow parameters were comparable in size, shape, intensity and liftoff height. Yet the LAR-Thick injector was able to stabilise a flame at a higher velocity ratio R_{max} of 0.60 in the absence of forcing, compared with 0.40 for the LAR-Thin injector, suggesting that a thicker wall enhanced flame anchoring. This difference may be attributed to the promotion of a recirculation zone associated with the thicker wall, enabling flame anchoring in a low-velocity region closer to the injector exit.

The influence of coaxial injector area ratio on flame blowoff resistance was investigated by examining the MAR-, LAR- and XLAR-Thick configurations at a fuel Reynolds number of 40 at various matching velocity ratios, with associated unforced flame images shown in figures 5(b), 5(d) and 5(e), respectively. While for velocity ratios of R = 0 and 0.11, all

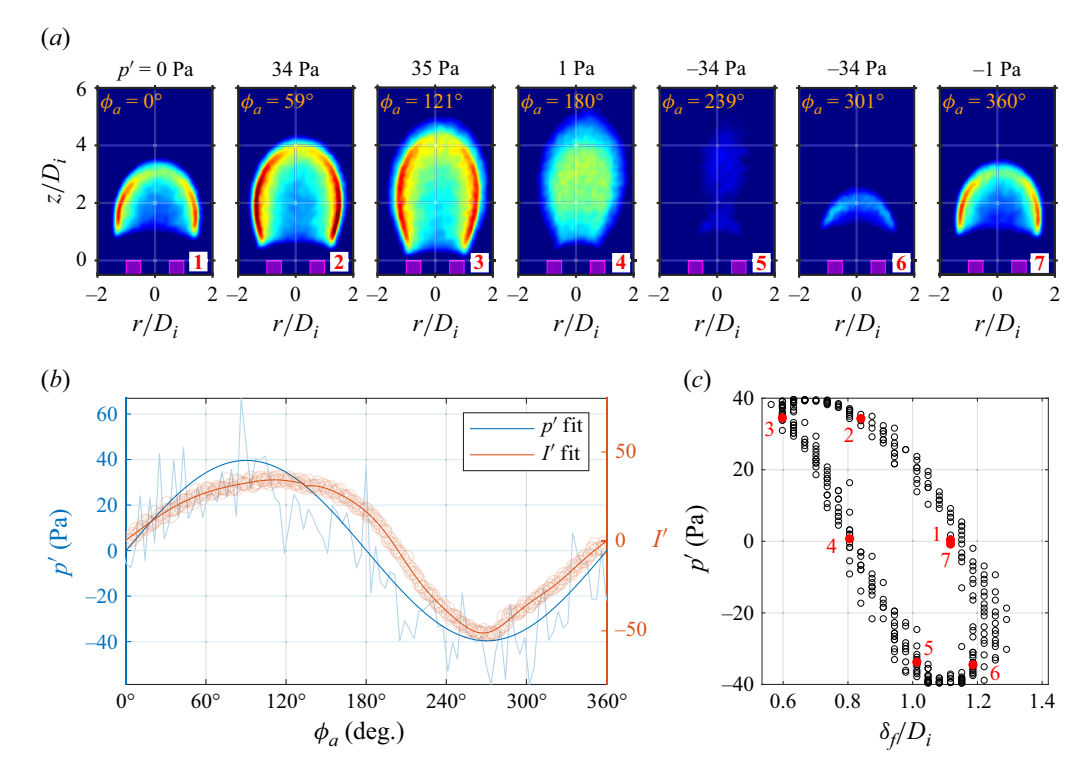


Figure 6. (a) Instantaneous flame images at equally spaced phases ϕ_a over an acoustic cycle, (b) phase-folded flame intensity fluctuation I' and pressure perturbation p' as a function of ϕ_a , and (c) dimensionless flame standoff distance δ_f/D_i versus p', where numbered red markers correspond to the visible images in panel (a). Data correspond to the Large-Thin single jet at Re = 20 under forcing conditions $f_a = 85$ Hz and $p'_{max} = 40$ Pa, producing SOC behaviour.

three injectors enabled clear flame anchoring (with the XLAR-Thick injector exhibiting strongest anchoring), at R = 0.33, all flames showed flame liftoff. The XLAR-Thick injector showed the greatest degree of flame standoff, suggesting it would be least robust to acoustic perturbations.

4. Forced acoustic-flame response

For both single and coaxial jets exposed to acoustic excitation at a PAN, the flame response exhibited distinct transitions in dynamical behaviour with increasing forcing amplitude. As will be shown and discussed in detail, three key acoustic–flame behaviours may be identified, and insights into the coupling dynamics and transitional behaviours of acoustically driven flames can reveal key injector design parameters promoting flame stability and resistance to blowoff.

4.1. Sustained oscillatory combustion (SOC)

Figure 6 presents the response of the Large-Thin single-jet injector to acoustic forcing conditions with $f_a = 85$ Hz and a measured pressure perturbation amplitude $p'_{max} = 40$ Pa. The flame here exhibited sustained oscillatory combustion, growing in vertical extent, then retracting and shrinking, always essentially maintaining flame anchoring in the vicinity of the jet exit plane. Figure 6(a) displays instantaneous flame images at equally spaced phases ϕ_a of the acoustic cycle with corresponding local p' measurements, with

numbering (1–7) corresponding to the images shown. These images revealed oscillations in flame shape, intensity and standoff distance with a period associated with the applied forcing frequency. The flame characteristics matched one another at ϕ_a of 0° and 360° , signifying motion with clear periodicity. The flame reached the lowest standoff distance when $\phi_a = 121^{\circ}$, corresponding to δ_f equal to $0.6D_i$; this coincided with conditions where the intensity and vertical extent of the flame were the largest. The highest liftoff height of $1.3D_i$ was achieved when the intensity of the flame was near its lowest magnitude. The liftoff dynamic at the fuel jet exit exhibited an overall oscillation amplitude of $0.7D_i$, which grew for more moderate SOC behaviours at higher forcing amplitudes. Figure 6(b)presents the spatially averaged flame intensity fluctuations I' plotted as a function of phase (per the examples in figure 6a), along with the recorded pressure perturbations p', highlighting their nearly synchronised behaviour. The phase-folded I' waveform was obtained by resampling the time series of I' based on the acoustic period, incorporating 341 instantaneous frames over 29 cycles for this acoustic frequency. Figure 6(c) illustrates the relationship between the non-dimensional flame standoff distance δ_f/D_i and p', with numbered red markers corresponding to the flame image series shown in figure 6(a). This single-loop representation effectively captured the periodic variation of flame standoff in response to the acoustic cycle over many acoustic cycles. This behaviour closely aligned with observations from AFRL studies on acoustically coupled turbulent flames at a PAN location, where the flame standoff distance reaches a minimum at the peak value of p' and a maximum standoff distance at the lowest p' or negative value relative to the mean chamber pressure (Plascencia et al. 2024a). Animations corresponding to the flame oscillations and flame standoff distance in figure 6 are shown in supplementary movie 1 available at https://doi.org/10.1017/jfm.2025.10701.

POD analysis served as the primary tool for distinguishing the characteristic dynamics under acoustically excited conditions, revealing distinct signatures associated with the flame's varying dynamical responses. POD results derived from the temporally evolving high-speed images corresponding to the conditions shown in figure 6 are presented in figure 7, where the cumulative POD modal energy of the four most dominant modes was well above 90 %. Figure 7(a) shows the four dominant POD mode structures, where the first mode represents global intensity fluctuations, containing $E_1 = 72 \%$ of the total energy. The next three modes were associated with the flame's liftoff oscillations. The power spectral density (PSD) of the POD temporal mode coefficients (a_1-a_4) , shown in figure 7(c), revealed peaks at the applied excitation frequency and its higher harmonics, consistent with flame/flow lock-in to the applied excitation. The POD mode coefficients, plotted against one another, produced the phase portraits shown in figure 7(b). The a_1-a_2 phase portrait formed a single-looped trajectory, representing a limit cycle-like periodicity, where the higher mode phase portraits exhibited more complex looped periodic and higher-harmonic behaviour, indicative of mode coupling. Animations corresponding to the POD mode structures in figure 7 with an additional 3-D phase portrait may be seen in supplementary movie 2. The POD characteristics observed here were consistent across all SOC cases, regardless of injector configuration, single or coaxial, with similar phase portraits, suggesting similar behaviour in the flame dynamics. For example, figure 8 presents the POD results for the SAR-Thin coaxial jet at $Re_1 = 20$ and R = 0.33, under forcing conditions of $f_a = 85$ Hz and $p'_{max} = 59$ Pa, and figure 9 presents the POD results for the LAR-Thick coaxial jet at $Re_1 = 40$ and R = 0.11, under forcing conditions of $f_a = 0.11$ 135 Hz and $p'_{max} = 201$ Pa. Both these results exhibited the distinct SOC characteristics similar to figure 7, with similar mode structures, 3-D phase portraits, and spectral peaks only at f_a and its higher harmonics. The a_1 - a_2 mode coefficient relationship was typically found to be strongly circular (periodic), and the other relations, two-dimensional

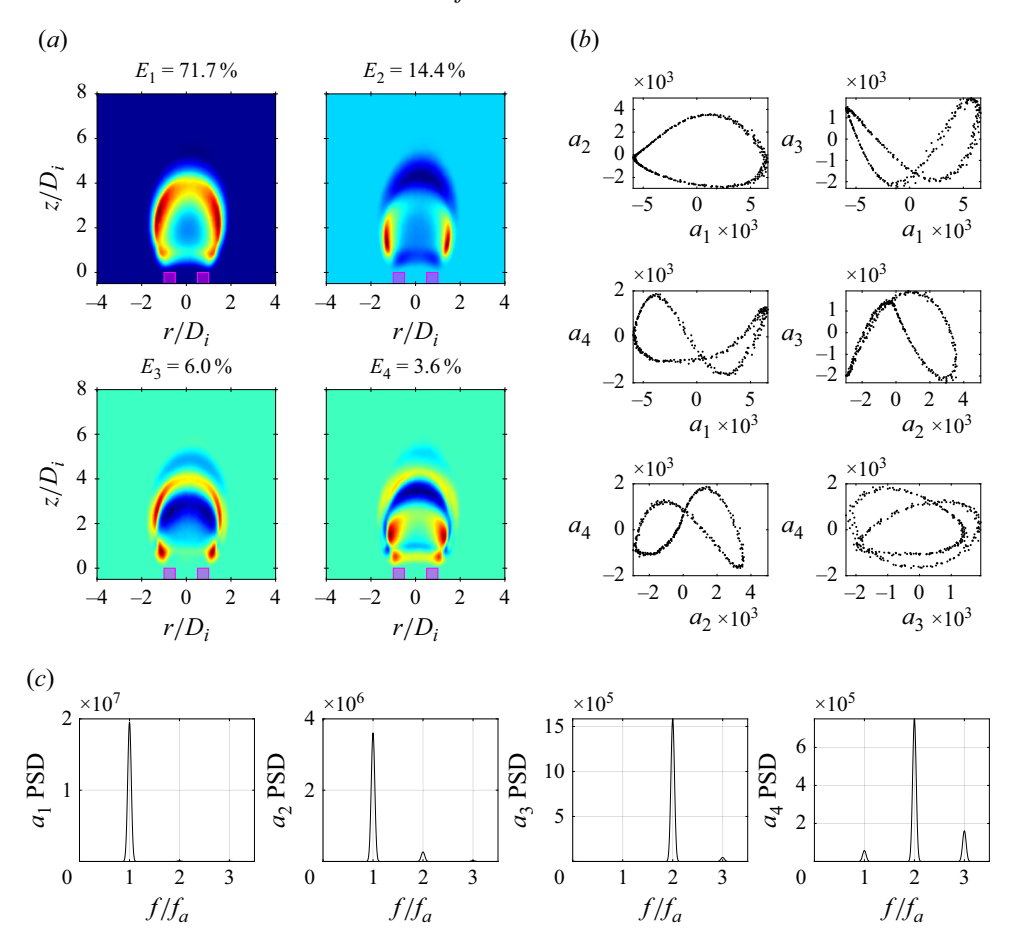


Figure 7. Results from POD analysis of flame images, including (a) the first four POD modes, (b) POD mode-based phase portraits and (c) mode spectra. Data correspond to the Large-Thin single jet at Re = 20 under forcing conditions $f_a = 85$ Hz and $p'_{max} = 40$ Pa, exhibiting SOC behaviour.

projections of the 3-D structures in figures 8(b) and 9(b), similarly showed trajectories reflective of the higher harmonics in the dynamics.

4.2. Periodic liftoff and reattachment (PLOR)

At higher excitation amplitudes for PAN forcing, both single- and coaxial-jet flames experienced periodic liftoff and reattachment (PLOR) behaviour, which was reminiscent of PLOR experienced by flames in the vicinity of a PN (Sim *et al.* 2020*b*; Vargas *et al.* 2023, 2025), but with important phenomenological differences. As an example, figure 10 shows the Large-Thin single jet flame behaviour at Re = 20 undergoing PLOR under forcing conditions of $f_a = 115$ Hz and $p'_{max} = 80$ Pa. The flame intensity and standoff distance oscillated primarily at the applied forcing frequency f_a , but exhibited a global liftoff and reattachment to the burner at a frequency of $f_a/2$. Unlike previous studies involving pressure node forcing of microjet flames (of various geometries) at 332 Hz, where the periodic flame liftoff frequency is significantly lower than the forcing frequency, lying in the range of 10–20 Hz and being dependent on p'_{max} , the periodic liftoff and reattachment frequency for a flame undergoing PLOR at a PAN was observed primarily at the subharmonic $f_a/2$, and was independent of p'_{max} . The instantaneous

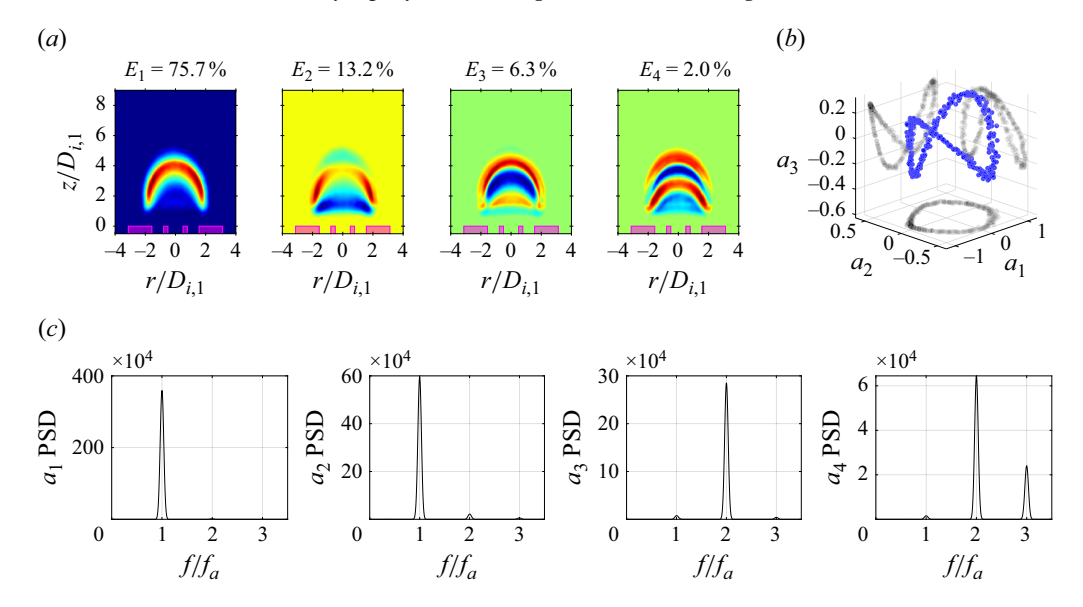


Figure 8. Results from POD analysis of flame images, including (a) the first four POD modes, (b) POD modebased 3-D phase portrait and (c) mode spectra. Data correspond to the SAR-Thin coaxial injector at $Re_1 = 20$ and R = 0.33 under forcing conditions $f_a = 85$ Hz and $p'_{max} = 59$ Pa, exhibiting SOC behaviour.

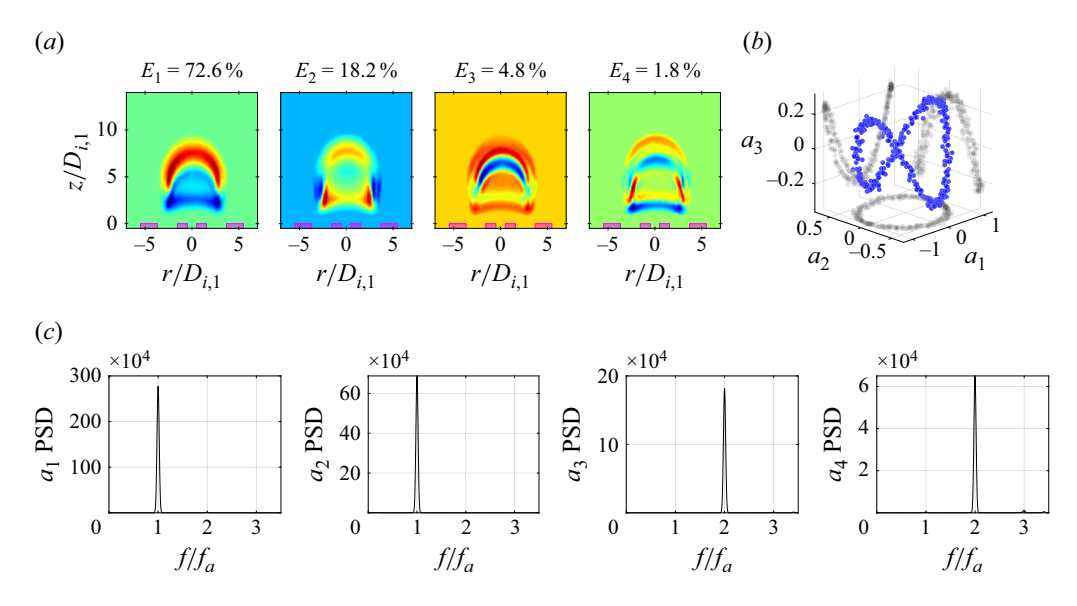


Figure 9. Results from POD analysis of flame images, including (a) the first four POD modes, (b) POD mode-based 3-D phase portrait and (c) mode spectra. Data correspond to the LAR-Thick coaxial injector at $Re_1 = 40$ and R = 0.11 under forcing conditions $f_a = 135$ Hz and $p'_{max} = 201$ Pa, exhibiting SOC behaviour.

flame image series shown in figure 10(a) shows this behaviour, spanning two applied acoustic cycles, with behaviour at acoustic phases running from 0° to approximately 720° . Results demonstrate the flame's bifurcated response, where flames were roughly similar in shape between phases that were 360° apart, but where the second cycle involved flames that were much more lifted, in general. Near the end of two acoustic cycles associated

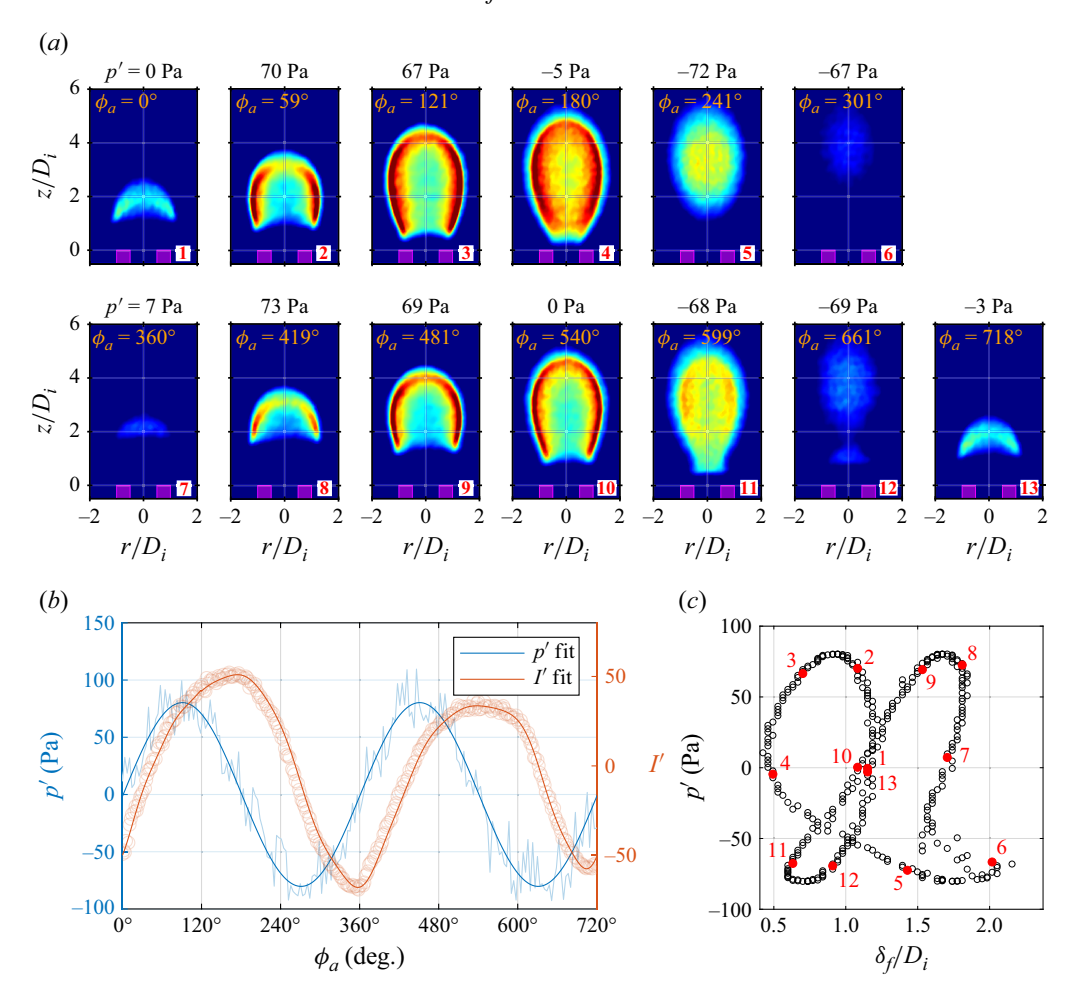


Figure 10. (a) Instantaneous flame images at equally spaced phases ϕ_a over an acoustic cycle, (b) phase-folded flame intensity fluctuation I' and pressure perturbation p' as a function of ϕ_a , and (c) dimensionless flame standoff distance δ_f/D_i versus p', where numbered red markers correspond to the visible images in panel (a). Data correspond to the Large-Thin single jet at Re = 20 under forcing conditions $f_a = 115$ Hz and $p'_{max} = 80$ Pa, exhibiting PLOR behaviour.

with the forcing frequency, the flames aligned well at $\phi_a = 0^\circ$ and approximately 720°, effectively doubling the overall period associated with flame dynamics. For each of the 360° cycles shown in figure 10(a), the flame reached its lowest standoff height when the intensity was at a maximum, and conversely, the highest liftoff when the intensity was minimal, as with SOC behaviour noted in § 4.1. However, for PLOR, the second complete cycle involved flames that were systematically at a higher liftoff height than during the first cycle. This additional periodic behaviour (liftoff) was demonstrated in figure 10(b), where the flame intensity I' waveform was not synchronised with the applied standing wave represented by the pressure perturbation. The phase lag between the fitted p' and I' was determined using FFT applied to the corresponding signals to extract phase angles at the forcing frequency, revealing the phase lag ($\Delta \phi$) of 75° between p' and I' for the case in figure 10. This phase lag represented an average value; nonlinear flame—acoustic interactions introduced variations in the instantaneous phase lag. Throughout the acoustic cycle, the instantaneous phase difference between the flame intensity and the

acoustic pressure oscillation fluctuated, shifting between values both smaller and larger than 90°. This variation in phase lag suggested possible periodic transitions between positive and negative Rayleigh index contributions to the integrand within the acoustic period, indicative of the changing nature of the thermoacoustic coupling. For instance, at $\phi_a = 0^\circ$, the phase lag was 29°, showing a somewhat in-phase response, which would contribute to a positive Rayleigh index. However, at $\phi_a = 180^\circ$, the phase lag increased to 96° between p' and I', which would contribute towards a negative Rayleigh index and thus a shift toward destructive coupling. In the second acoustic cycle, starting at $\phi_a = 360^{\circ}$, the phase lag was 67°, maintaining a positive Rayleigh index. By $\phi_a = 540^{\circ}$, the phase lag reached 105°, which would result in a negative Rayleigh index contribution again. This cycle of fluctuating instantaneous phase lag and alternating Rayleigh index terms may contribute to the complex behaviour of the PLOR flame response, where this dynamical relationship caused the flame to lift off and subsequently reattach as the phase relationship shifted, restoring conditions for stable anchoring, and then repeating in a cyclical fashion. The variation in flame standoff distance with local pressure perturbation amplitude, documented in figure 10(c), further illustrates the periodic liftoff and reattachment behaviour, highlighting the bifurcation in the frequency response. This is characterised by a double-loop trajectory with four distinct flame standoff distances δ_f/D_i for each p' value. During the first acoustic period, the flame's standoff distance initially dropped to a minimum of $0.5D_i$ at approximately $\phi_a = 180^\circ$, before rising to $2D_i$. At the start of the next acoustic period ($\phi_a = 360^{\circ}$), the standoff distance was $1.7D_i$, which was higher than the initial height of $1.1D_i$ at $\phi_a = 0^\circ$. The reattachment of the flame during the second acoustic cycle, occurring around $\phi_a = 600^{\circ}$, also occurred at a higher standoff of $0.6D_i$ compared with $0.5D_i$ at $\phi_a = 180^\circ$. The liftoff dynamic exhibited an overall oscillation amplitude of nearly $1.5D_i$, much larger than cases undergoing SOC. Animations corresponding to the flame oscillations and flame standoff distance in figure 10 may be seen in supplementary movie 3.

POD analysis may be applied to the images capturing flame dynamics associated with PLOR shown in figure 10. This POD analysis is shown in figure 11, revealing attributes that indicated the introduction of an additional time scale associated with the liftoff frequency. In figure 11(a), POD mode structures 1 and 2 were similar to those observed for SOC dynamics (e.g. as in figure 7a), but for the PLOR condition shown in figure 11(a), the introduction of the subharmonic periodic liftoff time scale appeared in modes 3 and 4, with additional structures within the overall flame zone, suggestive of additional relevant frequencies associated with the dynamics. The evidence for the additional frequency associated with a doubled period for flame response (i.e. the subharmonic) may be found in the mode coefficient's spectra, in figure 11(c). In these figures, spectral peaks at precisely the subharmonic frequency, $f_a/2$, the forcing frequency, f_a , as well as combinations of their higher harmonics were observed. This multi-frequency behaviour was further reflected in the phase portraits shown in figure 11(b), where the transition from SOC to PLOR introduced a two-phase liftoff cycle, resulting in double-loop trajectories, a distinct signature of the doubled-periodic flame response. Animations corresponding to the POD mode structures in figure 11 with an additional 3-D phase portrait may be seen in supplementary movie 4. Overall, these signatures were consistently associated with PLOR dynamics arising from PAN excitation, observed in both single and coaxial jets. For example, figure 12 presents the POD results for the SAR-Thin coaxial jet at $Re_1 = 20$ and R = 0.33, under forcing conditions of $f_a = 85$ Hz and $p'_{max} = 65$ Pa. The results exhibited PLOR characteristics similar to those in figure 11, with similar mode structures, a 3-D phase portrait showing two periodic orbits in each plane, and spectral peaks at $f_a/2$, f_a and their higher harmonics.

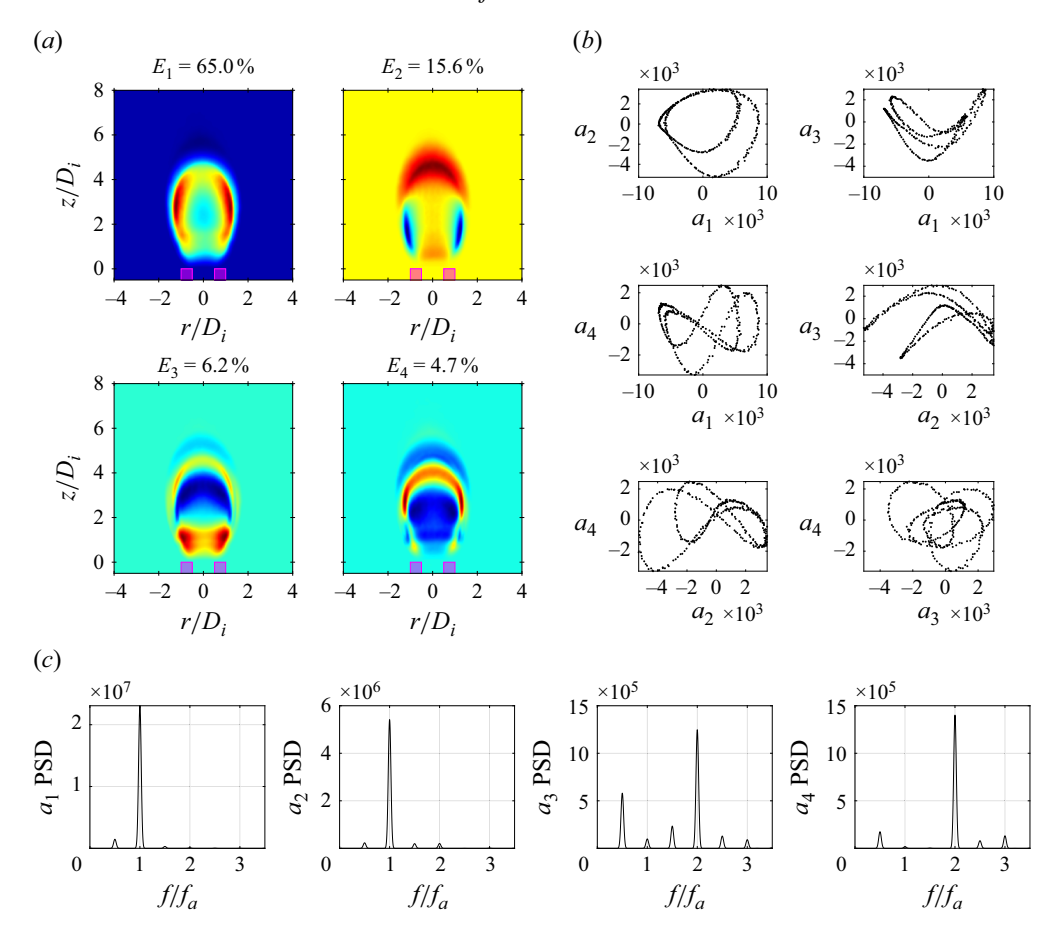


Figure 11. Results from POD analysis of flame images, including (a) the first four POD modes, (b) POD mode-based phase portraits and (c) mode spectra. Data correspond to the Large-Thin single jet at Re = 20 under forcing conditions $f_a = 115$ Hz and $p'_{max} = 80$ Pa, exhibiting PLOR behaviour.

We note, however, that PLOR was not observed for the coaxial jets operating at higher velocity ratios which produced a naturally lifted flame (e.g. for the lifted flame cases shown in figures 4 and 5). Moreover, among the coaxial jets with attached flame conditions under unforced conditions, there were a few instances where the PLOR frequency did not correspond to the subharmonic $f_a/2$ of the forcing frequency. It was found that for the coaxial jets under certain flow conditions (specifically, the SAR-Thin at $Re_1 = 10$ for R=0 and R=0.11, MAR-Thick at $Re_1=20$ for R=0, and LAR-Thin at $Re_1=20$ for R=0), a PLOR frequency of approximately 24 Hz was associated with the periodic liftoff of the flame, independent of forcing frequency and forcing amplitude. All these cases were very close to blowoff conditions (within approximately a 10 Pa increase of p'_{max}). As an example, figure 13 presents the POD results for the SAR-Thin coaxial jet flame at $Re_1 = 10$ and R = 0, which exhibited PLOR at 24 Hz when the flame was exposed to forcing conditions $f_a = 145$ Hz and $p'_{max} = 164$ Pa. Interestingly, this PLOR frequency was of similar order to those observed in pressure node excitation studies (Vargas et al. 2023, 2025), with comparable POD phase portraits and spectra showing dominance of the liftoff frequency over the applied forcing frequency, though in the case of forcing

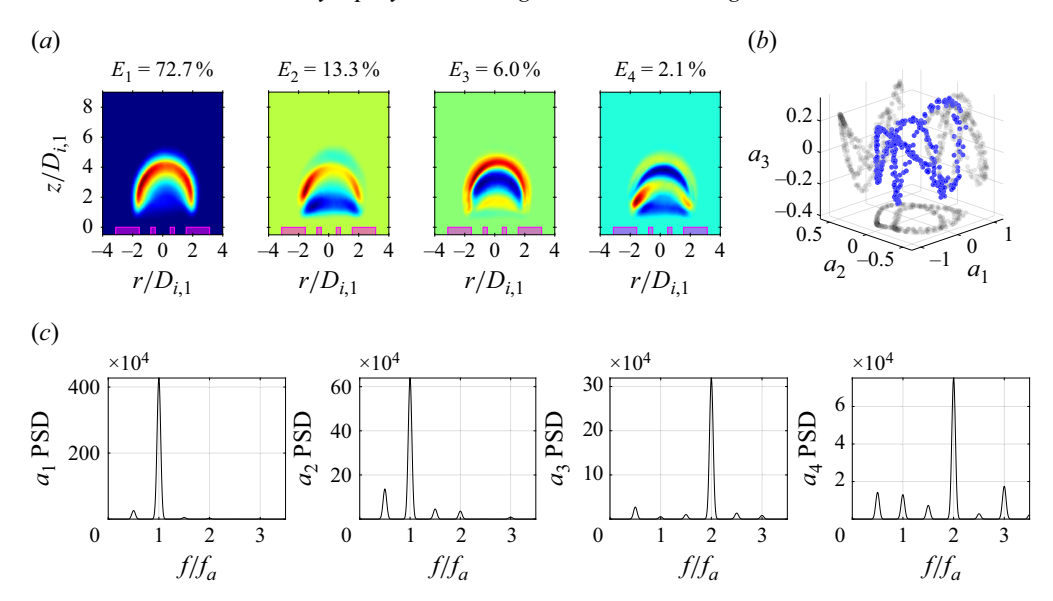


Figure 12. Results from POD analysis of flame images, including (a) the first four POD modes, (b) POD mode-based 3-D phase portrait and (c) mode spectra. Data correspond to the SAR-Thin coaxial injector at $Re_1 = 20$ and R = 0.33 under forcing conditions $f_a = 85$ Hz and $p'_{max} = 65$ Pa, exhibiting PLOR behaviour.

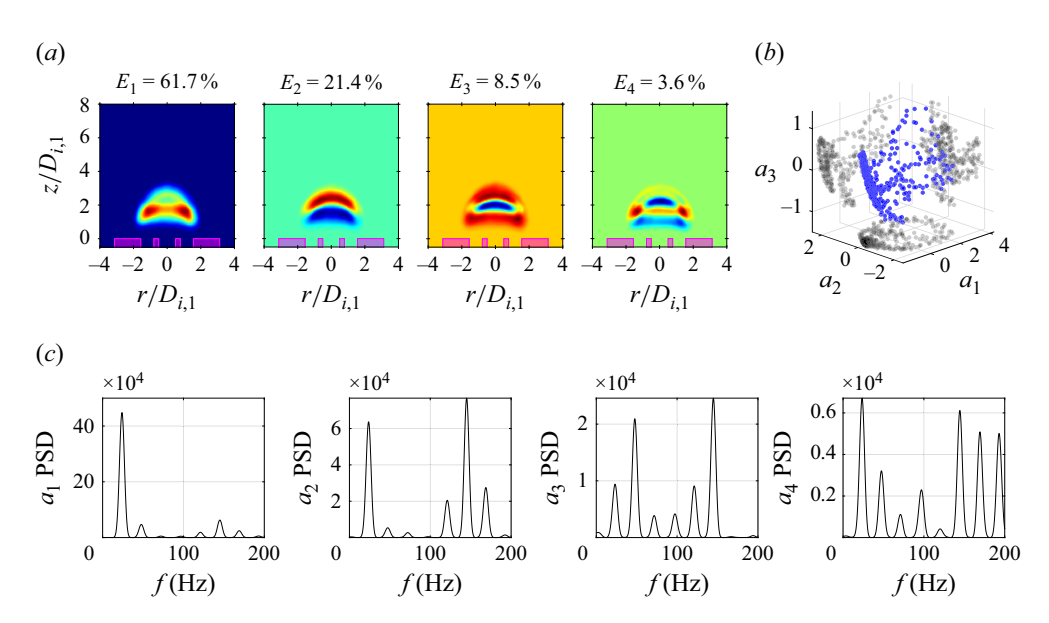


Figure 13. Results from POD analysis of flame images, including (a) the first four POD modes, (b) POD modebased 3-D phase portrait and (c) mode spectra. Data correspond to the SAR-Thin coaxial injector at $Re_1 = 10$ and R = 0 under forcing conditions $f_a = 145$ Hz and $p'_{max} = 164$ Pa, exhibiting PLOR behaviour at 24 Hz.

near a PN, there is transverse deflection and periodic liftoff of the flame in the transverse deflection direction.

The transitions in dynamical characteristics, along with distinct phase portraits and spectral signatures, play a crucial role in understanding instability transitions in acoustically coupled combustion. As an additional means of exploring the gradual

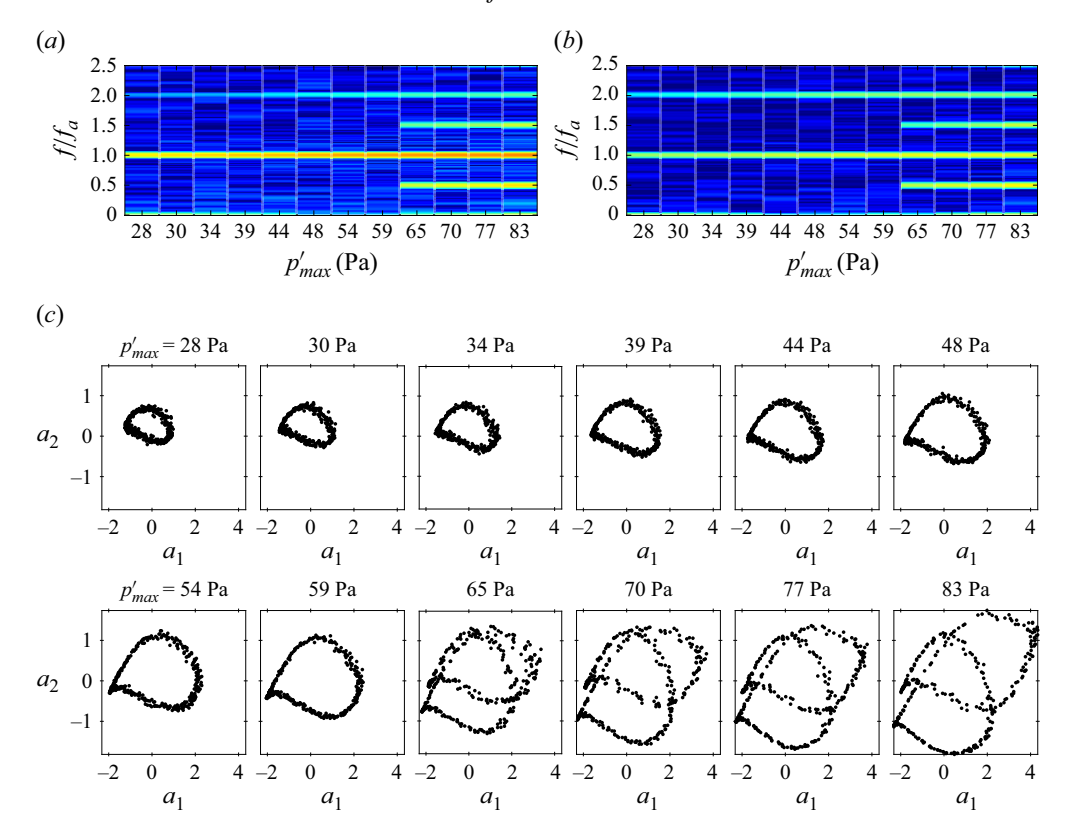


Figure 14. POD results for the SAR-Thin coaxial jet with $Re_1 = 20$ and R = 0.33 under acoustic forcing at frequency $f_a = 85$ Hz with p'_{max} ranging from 28 to 83 Pa. Shown in panels (a) and (b) are spectrograms of the POD temporal mode coefficients a_1 and a_2 , and in (c) phase portraits associated with each step in p'_{max} .

transition with increasing excitation amplitude, figure 14 presents the POD results for the SAR-Thin coaxial jet with $Re_1 = 20$ and R = 0.33 under acoustic forcing at fixed frequency $f_a = 85$ Hz and with successively increasing p'_{max} ranging from 28 to 83 Pa. Figures 14(a) and 14(b) show POD coefficient spectrograms associated with the strength of the mode 1 and 2 coefficients, respectively, with increasing pressure amplitude, while figure 14(c) shows the POD phase portraits based on modes 1 and 2 as pressure increases. The transition from SOC to PLOR at $p'_{max} = 65$ Pa (the case shown in figure 12) was clearly visible in the rather abrupt emergence of a new spectral peak at $f/f_a = 0.5$ in the mode coefficients in figures 14(a) and 14(b), and in the abrupt formation of a double-loop trajectory in the phase portrait in figure 14(c). Similar transitions in such metrics were observed for other cases undergoing the transition from SOC to PLOR behaviour. These inherent dynamical features thus can provide valuable insights into the transition process and its prediction, even when only two POD modes are considered.

4.3. Permanent flame liftoff (PFLO)

By further increasing the pressure amplitude, the forced flames in some cases entered a permanently lifted state of oscillation while avoiding flame blowoff. With increasing forcing amplitude after permanent lifting was achieved, the flame standoff distance grew with the increased forcing amplitude until the flame ultimately reached blowoff. Figure 15 shows an example of the response of the Large-Thin single-jet flame at Re = 20 undergoing

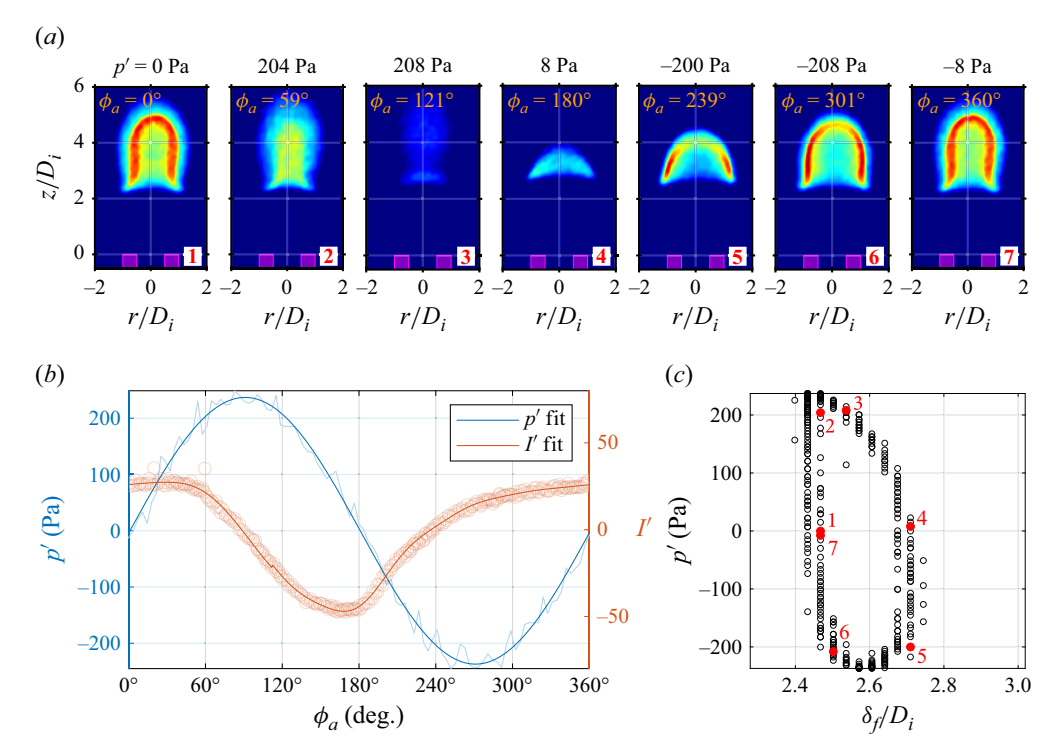


Figure 15. (a) Instantaneous flame images at equally spaced phases ϕ_a over an acoustic cycle, (b) phase-folded flame intensity fluctuation I' and pressure perturbation p' as a function of ϕ_a , and (c) dimensionless flame standoff distance δ_f/D_i versus p', where numbered red markers correspond to the visible images in panel (a). Data correspond to the Large-Thin jet at Re=20 under forcing conditions $f_a=165$ Hz and $p'_{max}=237$ Pa, exhibiting PFLO behaviour.

permanent flame liftoff under forcing conditions of $f_a = 165$ Hz and $p'_{max} = 237$ Pa. The flame intensity and standoff distance, shown for one acoustic cycle in figure 15(a), oscillated at the applied forcing frequency. This observation was verified by the variation in I' in figure 15(b) and the single-loop trajectory in figure 15(c), with an average phase lag of 254° observed between the p' and I' waveform. The flame was permanently detached from the burner in an oscillatory lifted state, with a minimum and maximum standoff distance of $2.4D_i$ and $2.7D_i$, respectively. For these lifted flame cases, the oscillations in standoff distance were much smaller and occurred at higher excitation frequencies compared with conditions undergoing SOC or PLOR, where the flame in figure 15 exhibited an oscillation amplitude of only $0.3D_i$. For PFLO flame dynamics, the flame oscillated only at the applied frequency, resulting in POD results such as those in figure 16, with a similarity to those of SOC, just with the mode structures captured in a lifted state. The mode coefficient spectra exhibited pronounced peaks only at the applied forcing frequency and its higher harmonics (e.g. figure 16c), and the phase portraits revealed singular, modecoupled trajectories (figure 16b), as for SOC cases. Animations corresponding to figures 15 and 16 may be seen in supplementary movies 5 and 6, respectively.

For an alternative coaxial jet case with PFLO behaviour, figure 17 presents the POD results for the LAR-Thick coaxial jet at $Re_1 = 40$ and R = 0.11, under forcing conditions of $f_a = 135$ Hz and $p'_{max} = 311$ Pa. Again, the dynamics captured in the POD analysis were consistent with the prescribed PFLO characteristics similar to figure 16, with similar mode structures and spectral peaks. The phase trajectories are represented in a 3-D plot

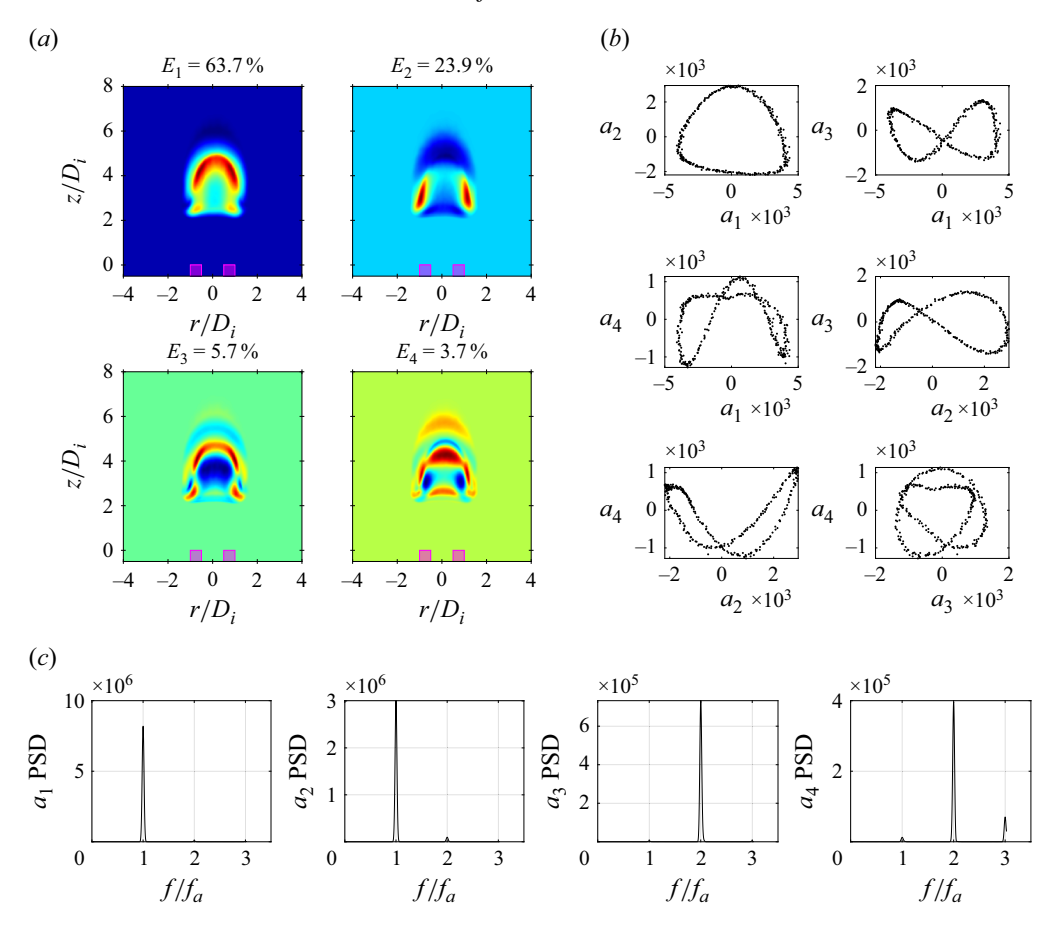


Figure 16. Results from POD analysis of flame images, including (a) the first four POD modes, (b) POD mode-based phase portraits and (c) mode spectra. Data correspond to the Large-Thin single jet at Re = 20 under forcing conditions $f_a = 165$ Hz and $p'_{max} = 237$ Pa, exhibiting PFLO behaviour.

(figure 16b), revealing much simpler periodicity in each plane than was seen for PLOR behaviour in figures 12 and 13. Figure 18 presents the POD phase portraits for the same case, the LAR-Thick coaxial jet with $Re_1 = 40$ and R = 0.11 under acoustic forcing $f_a = 135$ Hz, but with p'_{max} ranging from 167 to 359 Pa, producing transition from SOC to PFLO. These transitions in dynamical characteristics were initially thought to be difficult to predict, as there was no transition related to spectral signatures for SOC and PFLO in the acoustic–flame behaviour. Yet the phase portraits offer valuable insights, showing a progressive evolution in the size of the trajectory path, including an amplitude growth leading up to a maximum just before the transition to PFLO, which was documented to start at $p'_{max} = 292$ Pa. After this point, with an increase in excitation amplitude, the flames then further exhibited changes in orientation as well as the magnitude of the mode coefficients a_1 and a_2 .

5. Characterising underlying mechanisms, trends and response regimes

5.1. Frequency effects on flame oscillation amplitude

The present experiments explored microjet flame responses to PAN excitation for a wide range of flow conditions (indicated in tables 2 and 3) as well as forcing frequencies and

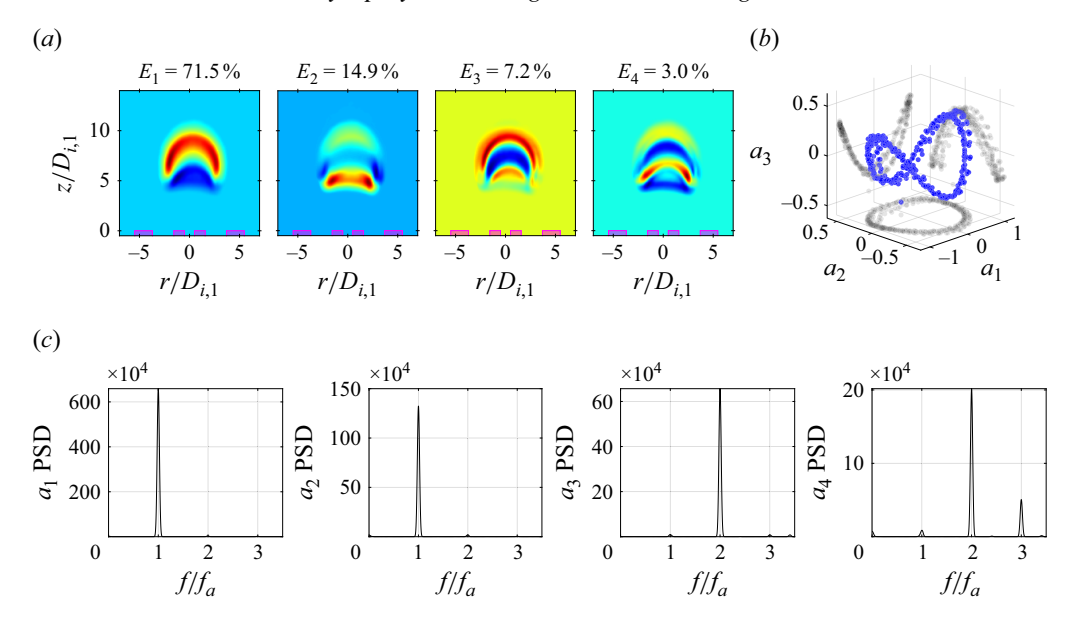


Figure 17. Results from POD analysis of flame images, including (a) the first four POD modes, (b) POD mode-based 3-D phase portrait and (c) mode spectra. Data correspond to the LAR-Thick coaxial injector at $Re_1 = 40$ and R = 0.11 under forcing conditions $f_a = 135$ Hz and $p'_{max} = 311$ Pa, exhibiting PFLO behaviour.

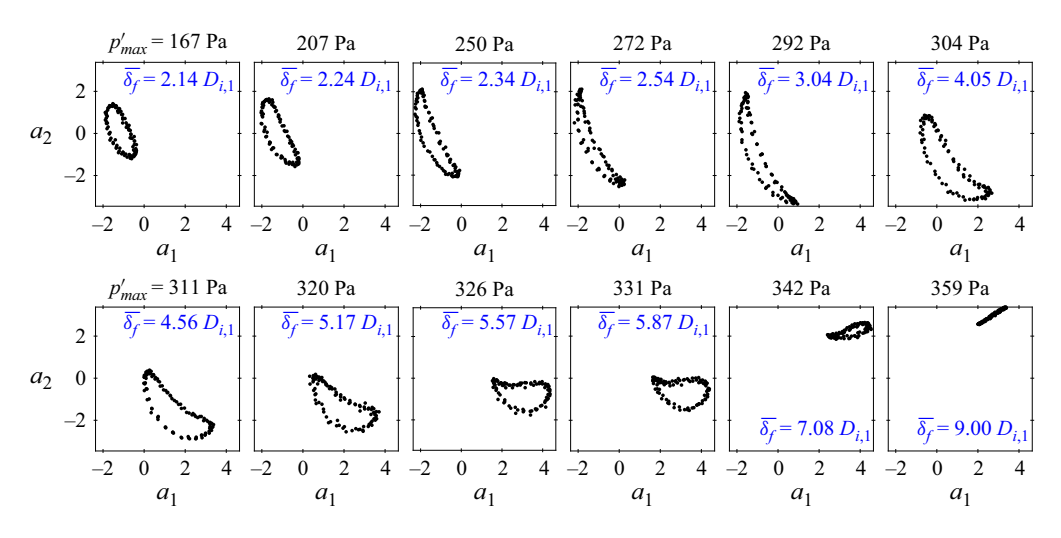


Figure 18. POD phase portraits for the LAR-Thick coaxial jet with $Re_1 = 40$ and R = 0.11 under acoustic forcing $f_a = 135$ Hz and p'_{max} ranging from 167 to 359 Pa, with corresponding mean standoff distance δ_f listed, transitioning from SOC to PFLO at 292 Pa.

amplitudes. Investigating the effect of varying forcing frequencies revealed their influence on flame oscillation amplitude and provided insights into the underlying response regimes. Figure 19 summarises the mean flame height $(\overline{\delta}_h)$ and mean standoff distance $(\overline{\delta}_f)$ in blue for the Large-Thin single jet across various forcing frequencies at the highest achieved value of p'_{max} just before flame blowoff. Shown in black are conditions corresponding to p'_{max} values producing SOC, PLOR and PFLO behaviour for these flames. For Re = 8 in figure 19(a), SOC occurred only at low frequency excitation, then PLOR response first

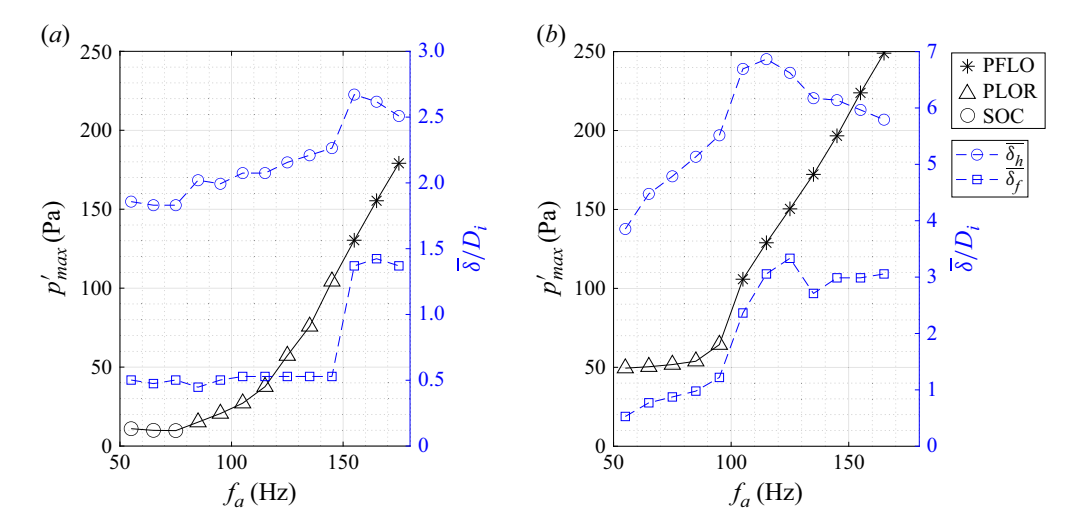


Figure 19. Mean flame height $\overline{\delta_h}$ and standoff distance $\overline{\delta_f}$ (both shown in blue) at the highest achieved p'_{max} conditions, just before flame blowoff, for the Large-Thin single jet at (a) Re = 8 and (b) Re = 20 for a range of forcing frequencies. Also shown are the respective p'_{max} conditions producing SOC, PLOR and PFLO (in black).

appeared at 85 Hz, indicated by the black triangle markers, and PFLO was initiated for frequencies at or beyond 155 Hz. Clearly, higher amplitudes of acoustic excitation could be accommodated by flames excited at higher excitation frequencies for both these singlejet cases, consistent with observations by Plascencia et al. (2024a) for PAN excitation. Here, $\overline{\delta}_f$ remained essentially constant at $0.5D_i$ when forcing frequency was increased from approximately 50 to 145 Hz, during which the flame exhibited SOC and then PLOR at increasing p'_{max} values. At this point, PFLO began, marked by a noticeable increase in the mean flame standoff distance $\overline{\delta_f}$ with increasing frequency, in addition to a rapid increase in the highest achieved p'_{max} value before blowoff. While the maximum p'_{max} value which the flame could withstand continued to increase with forcing frequency, the approximate $\overline{\delta_f}$ value converged to approximately 1.4 D_i , suggesting that higher forcing frequencies required larger p'_{max} to achieve similar flame standoff distances associated with PFLO, beyond which higher amplitude forcing would lead to flame blowoff. While the mean flame height δ_h was roughly constant during SOC behaviour, in the regime where PLOR response first appeared, approximately 85 Hz, $\overline{\delta_h}$ increased with f_a , indicating that the flame reached greater heights at higher forcing frequencies f_a and p'_{max} . The maximum flame height occurred just at PFLO initiation at 155 Hz, beyond which it started to decline. For Re = 20 in figure 19(b), similar trends were observed, though SOC did not occur in the forcing regime shown, and there were transitions at different frequencies and with different standoff distances as compared with the low-Re case in figure 19(a). For example, in figure 19(b), PFLO began at 105 Hz, which again corresponded to a sudden increase in $\overline{\delta_f}$, while $\overline{\delta_f}$ near blowoff consistently converged to approximately $3D_i$. The flame height $\overline{\delta_h}$ increased with forcing frequency where the flame height peaked at approximately $7D_i$ at 115 Hz, though once PFLO began, the maximum flame height decreased with a further increase in forcing frequency. These transitions may have occurred because, as the acoustic period T shortens, there would be less time for buoyant and hydrodynamic forces to drive flame oscillations, potentially reducing the oscillation amplitude. The underlying mechanisms of the frequency influence on the flame-acoustic interaction were consistent

across all excitation and flow conditions for both single and coaxial jets; results for the latter may be found from Hayrapetyan (2025).

5.2. Linking response regimes to the Rayleigh index

Understanding the interaction between acoustic waves and unsteady heat release is essential for analysing acoustically coupled flame stability. As mentioned previously, the Rayleigh criterion (Rayleigh 1896) can serve as a key principle in this assessment, where the Rayleigh index (1.1) helps pinpoint regions of stability and instability in acoustically forced flames by incorporating the phase and magnitude of this coupling. In estimating the Rayleigh index associated with a small region or volume enclosing an acoustically coupled flame, time-resolved pressure fluctuation measurements and OH* chemiluminescence intensity fluctuations, serving as a proxy for heat release rate fluctuations, are often incorporated (Sevilla-Esparza et al. 2014; Bennewitz et al. 2018; Sim et al. 2020a). Yet in the present gas-phase experiments, high-speed imaging is limited by the short exposure time between the imaging frames, combined with the low light emission from the flame's OH* chemiluminescence, resulting in significant signal dropout and noisy measurements for I'. To attempt to overcome this issue, limited high-speed OH* chemiluminescence imaging was performed to assess the extent of the difference between using visible-light intensity fluctuations to represent I' as a substitute for I'extracted from OH* chemiluminescence in calculating the Rayleigh index. The present OH* chemiluminescence imaging was captured with the use of a U-330 bandpass filter for comparison with high-speed visible imaging results.

Figures 20(a) and 20(b) compare the instantaneous OH* and visible image series, respectively, sequentially over comparable phases of the acoustic cycle, for the Large-Thin single-jet flame under forcing conditions $f_a = 155$ Hz and $p'_{max} = 158$ Pa. The OH* chemiluminescence imaging was denoised in an attempt to counteract the significant signal dropout caused by the bandpass filter and the spectral response of the camera sensor. This signal loss is evident in the image series, and in the lower maximum intensity of the colourbar in figure 20(a) compared with the visible-light images in figure 20(b). Yet the image series between the two sets exhibited strong alignment in both shape and intensity fluctuation at matching acoustic phases, ensuring consistency in temporal and spatial correlation. To assess whether visible-light imaging could be a suitable substitute for the OH* signal in estimating the Rayleigh index, the intensity fluctuation waveform I'was plotted for both diagnostics as a function of phase, along with the local measurement of p'; these are compared in figure 20(c). While the amplitudes of pressure and intensity fluctuations influence the magnitude of the Rayleigh index, it is the phase difference between the two that determines whether the interaction is constructive, leading to the growth of acoustic instabilities, or supposedly destructive, resulting in damping of the instability (Rayleigh 1896), or experiencing a change in the dynamic/combustion character (Sevilla-Esparza et al. 2014; Bennewitz et al. 2018; Sim et al. 2020a). The results in figure 20(c) show minimal differences between the normalised I' for the two imaging sets, despite greater uncertainty in the OH^* -based I' values, hence indicating a consistent behaviour for the two diagnostics. This suggests that the present visible-light imaging could be a suitable alternative to OH* chemiluminescent imaging in estimating the Rayleigh index under these relatively low frequency excitation conditions, where the visible-light I' can serve as a proxy for heat release rate fluctuations q'.

Before evaluating the Rayleigh index G for the current experiments, it is noted that the phase difference between p' and I' is an important component of combustion–acoustic coupling and can be easily quantified. Here, the PAN excitation in the waveguide acted to

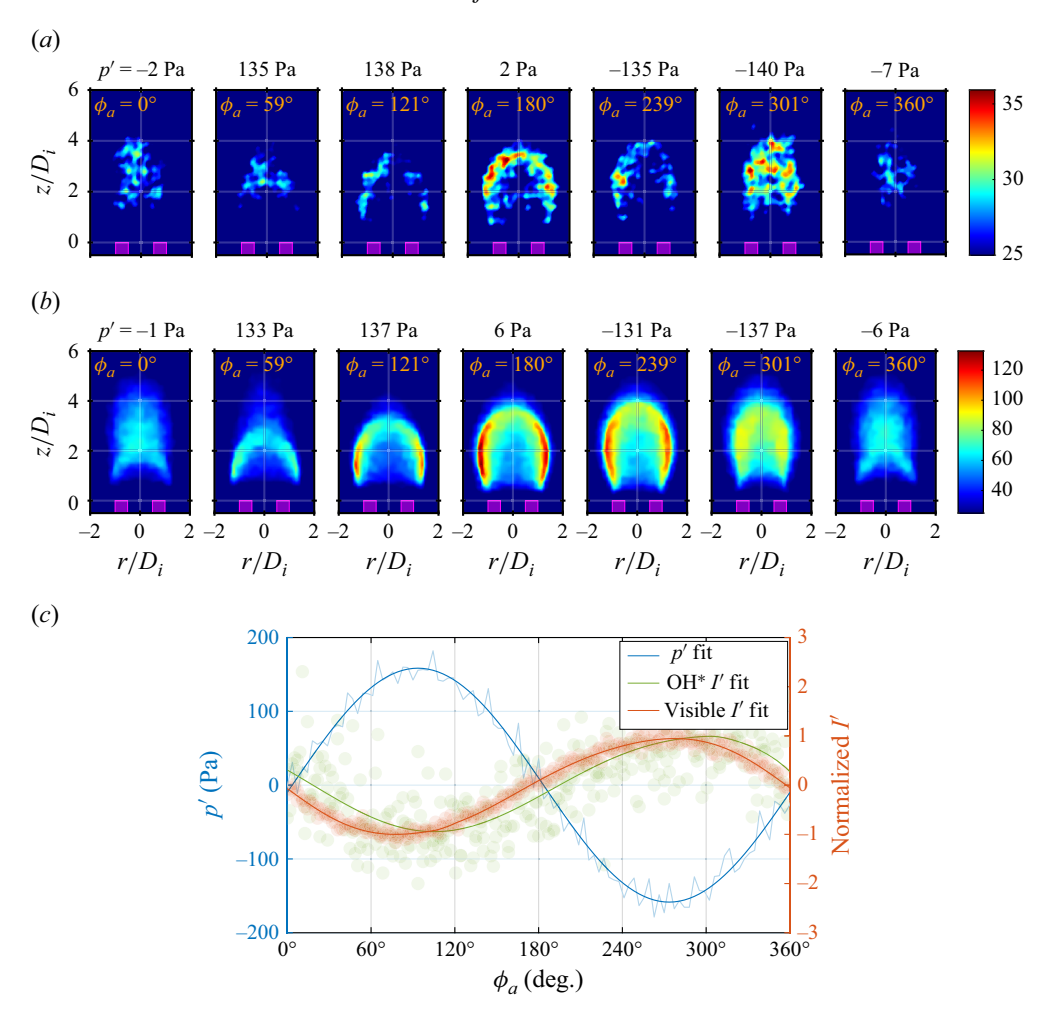


Figure 20. High-speed (a) OH* chemiluminescence and (b) visible-light images acquired at 1000 FPS for the Large-Thin single jet at Re = 20 under forcing conditions $f_a = 155$ Hz and $p'_{max} = 158$ Pa, exhibiting SOC behaviour. The phase-folded I' waveform for panels (a) and (b) is plotted with p' as a function of phase ϕ_a in panel (c).

induce local perturbations in the local surrounding pressure and hence the fuel flow rate at the jet exit, as evidenced by oscillations in flame size and intensity (e.g. as in figures 6 or 10), limited schlieren analysis of the cold jet, and upstream flowmeter observations of flow disturbances (Hayrapetyan 2025). The phase lag between recorded pressure perturbations p' and flame intensity fluctuations I', e.g. as seen in the plots in figure 20(c), reflected differences among the propagation speeds of the acoustic disturbances, fuel and oxidiser fluid mechanical transport and flow structures, and chemical reaction processes at the flames. Figure 21 summarises the average phase lag $\Delta \phi$ for the four single-jet geometries explored here at Re = 20 for a range of excitation pressures and frequencies. These data are plotted in the range $\pm 180^\circ$, and reveal interesting trends. Figure 21(a) shows an example of the average phase lag as a function of p'_{max} associated with SOC, PLOR and, if it occurs, PFLO, for a fixed forcing frequency $f_a = 135$ Hz. Here, we note that a fixed Re value implied a higher fuel jet velocity for the smaller diameter single jets (e.g. Small-Thin or Small-Thick) than for the larger diameter jet (e.g. Large-Thin). For lower fuel velocities,

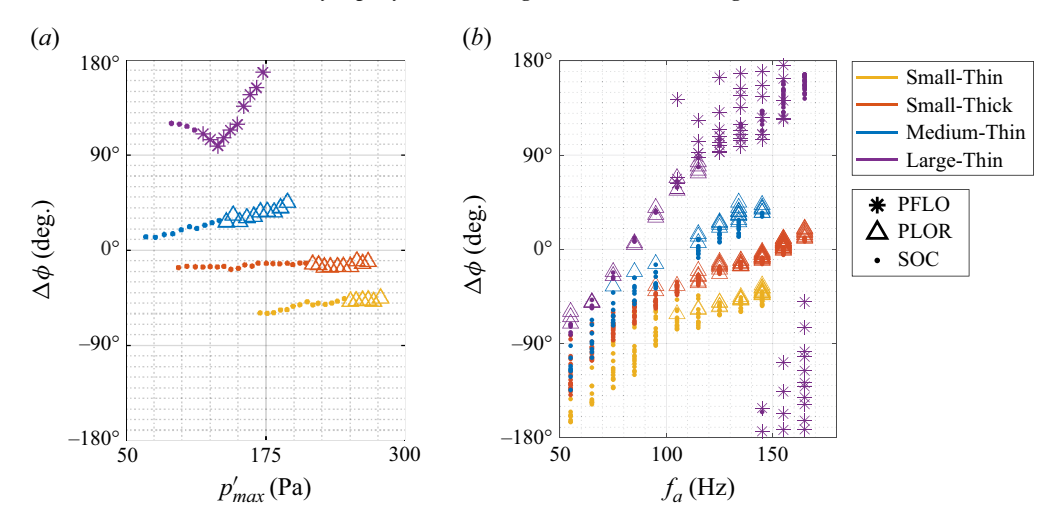


Figure 21. Average phase lag $\Delta \phi$ between visible-light intensity fluctuation I' waveform and pressure perturbation p' for the various single jets at Re=20 for (a) $f_a=135$ Hz as a function of p'_{max} associated with SOC, PLOR and PFLO, and (b) average phase lag $\Delta \phi$ as a function of forcing frequency for various p'_{max} values.

the time delay for fuel transport, and consequently the phase lag, would be expected to be larger, which is consistent with the Large-Thin injector result in figure 21(a). In contrast, for higher fuel velocities (e.g. the Small-Thin injector), the time delay for fuel transport would be smaller, producing a smaller phase lag in the flame dynamics. This behaviour was also verified in figure 21(a). It is also noted that the phase lag remained largely unchanged for SOC and PLOR cases with increasing p'_{max} , yet for PFLO cases (*), in figure 21(a), seen for the Large-Thin injector, the phase lag began to significantly increase with p'_{max} after transition. Figure 19(b) indicates that the Large-Thin PFLO condition at $f_a = 135$ Hz and $p'_{max} = 175$ Pa had a flame standoff distance of $2.7D_i$; per figure 21(a), this condition produced the largest phase lag. These observations are consistent with the notion that the higher flame standoff associated with PFLO correlated with an increased convective distance for the fuel, creating a longer time delay or phase lag between the flow and reaction processes. Figure 21(b) shows a summary of the average phase lag as a function of forcing frequency for the various single-jet injectors and for different acoustic flame responses. Phase lag was observed to increase with higher frequency excitation; this was likely due to the shorter acoustic period T, since the effective time delay would otherwise remain constant for a given fuel injection velocity. The plot exhibited a diagonal trend, indicating that as the forcing frequency approached zero, the phase shift converged towards -180° , i.e. with fluctuations in pressure and velocity out of phase with respect to one another. This actually would be expected, as the moment of highest pressure at the jet exit momentarily reduces the flow velocity, leading to a decrease in fuel injection at that instant, causing I' to be at its minimum. The PFLO cases showed significant deviation from the general trend, however, where in some instances at $f_a = 145$ Hz and above, the phase lag exceeded 180°, and thus was plotted as being negative and resulted in a delayed response of nearly a full acoustic cycle.

Notably, the PLOR and PFLO response exhibited distinct phase-dependent behaviours in response to acoustic forcing. The PLOR behaviour, shown by the triangles in figure 21, was observed exclusively to have an average phase lag within the range of $\pm 90^{\circ}$,

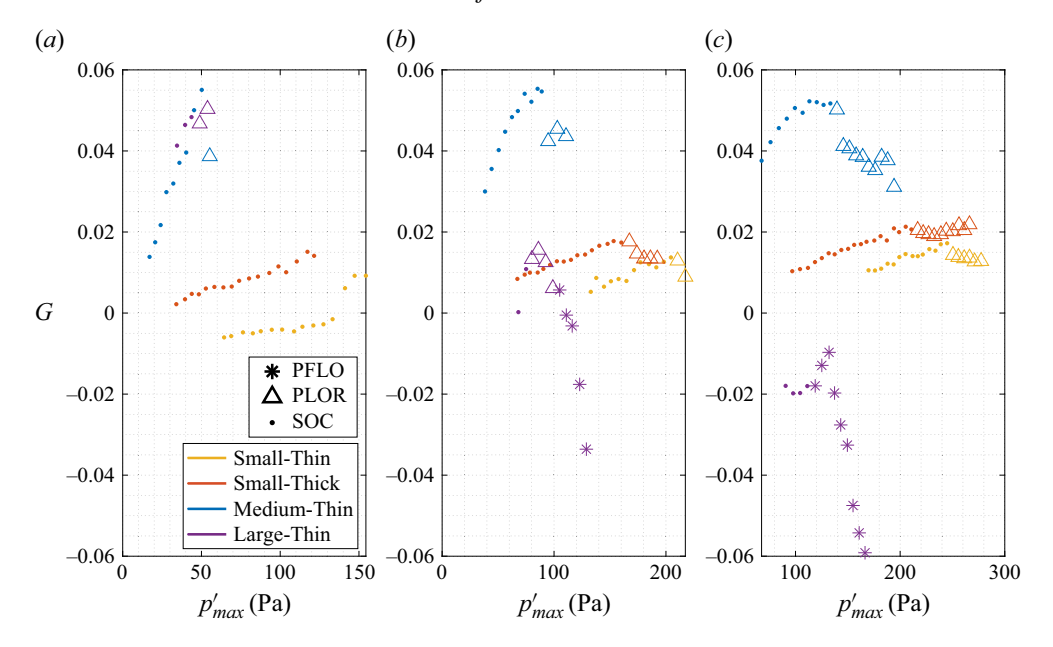


Figure 22. Rayleigh index as a function of p'_{max} associated with flame transitions (SOC, PLOR, PFLO) for the different single jets at Re = 20 for forcing frequencies (a) $f_a = 85$ Hz, (b) $f_a = 115$ Hz and (c) $f_a = 135$ Hz.

coinciding with an overall positive Rayleigh Index. In contrast, PFLO tended to primarily exist outside of the range of $\pm 90^{\circ}$, where the Rayleigh index would become negative, presumably dampening the instability or representing a major transition in the instability. This out-of-phase characteristic could be an indicator of the condition that prevented complete blowoff, allowing the flame to persist in a permanently lifted state. Similar kinds of trends to those in figures 21(a) and 21(b) were observed for coaxial jet dynamics. Such trends are relevant to understanding the influences of flow and excitation parameters on the Rayleigh index.

$$G = \frac{1}{T} \int_0^T \left(\frac{p'(t)}{p'_{max}}\right) \left(\frac{I'(t)}{I_o}\right) dt.$$
 (5.1)

As noted earlier, although the Rayleigh index G is typically used to indicate whether instabilities are amplified or damped, in the current experiments, a switch to negative Rayleigh index could represent a transition in the instability, as occurred in acoustically coupled droplet combustion experiments (Sevilla-Esparza *et al.* 2014; Bennewitz *et al.* 2018). In the present experiments, a normalised Rayleigh index, as defined in (5.1), was calculated and plotted in figure 22 as a function of p'_{max} (with flame transitions from SOC to PLOR or PFLO) for the four single jets at Re = 20 for three different forcing frequencies. The normalisation of intensity I_0 was defined by the intensity of the unforced flame imaged at 30 FPS, examples for which are in figure 3. The results for Rayleigh index in figure 22 correlated well with the phase lag summary in figure 21, as expected, where positive values of G were observed for cases with p' and I' waveforms having a phase lag lying within $\pm 90^{\circ}$, and negative values of G for more out-of-phase waveforms, with a phase lag above $+90^{\circ}$ or below -90° . An increase in the magnitude of G occurred with increased p'_{max} for all SOC cases, though it is noted that the Small-Thin injector showed a negative Rayleigh index at the lower frequency excitation in figure 22(a), consistent with the phase

lag in figure 21(b), though the flame oscillations were clearly present. Here, G became positive with increasing excitation amplitude p'_{max} as well as frequency. Once the fuel jet transitioned to PLOR or PFLO, a reversal in this trend occurred. For PLOR, a decrease in G was then observed, though it remained positive, due to the shift between in-phase and out-of-phase heat release rate with the acoustic cycle, as discussed in § 4.2. The PFLO cases, seen for the Large-Thin single jet, exhibited a transition to negative values of G from initially positive G for 115 Hz excitation at lower amplitudes (figure 22b), but which was consistently negative for all amplitudes during 135 Hz forcing (figure 22c). In both cases, these results, and those in figure 21(b), corresponded to a reduction in the oscillation magnitude when the flame became permanently lifted, as discussed in § 4.3 in connection with results in figure 15. It is also noted that, for higher frequency excitation of the Large-Thin single injector in figure 22(c), blowoff occurred at a much lower excitation pressure than for the other injectors, suggesting lower flame stability for such PFLO conditions. In fact, the other three single jets, with smaller inner diameters and higher jet velocities for the fixed Reynolds number, did not produce a permanently lifted flame in the frequency range explored; if it had been possible to produce higher frequencies in the experimental apparatus, PFLO might have been achieved.

6. Impact of key design parameters on flame stability

This study explored the influence of inner jet diameter, fuel Reynolds number, inner wall thickness, coaxial velocity ratio and area ratio on flame response, attachment, and overall resilience to a wide range of forcing frequencies and amplitudes. Extensive datasets were collected for the four single jets, covering the flow conditions shown in figure 3, and the five coaxial jets, covering the conditions shown in figures 4 and 5. Characteristic transitions in flame-acoustic coupling dynamics took place in very similar ways among the different injectors, and range of flow and excitation conditions, though with specific quantitative differences. Sample summary results for the response of different single fuel jet geometries under different flow and excitation conditions are shown in figure 23(a-d). The figures may be summarised notionally in figure 23(e), which maps the various flame response regimes observed as a function of the acoustic forcing frequency and pressure perturbation amplitude. Transition boundaries between these regimes are denoted by (\triangle) for SOC to PLOR, (*) for transition to PFLO and (\times) for transition to BO, where the dashed lines indicate approximate boundaries between these transitions. This notional response chart is relevant to both single- and coaxial-jet geometries; additional examples of such diagrams for different injectors, flow conditions and excitation conditions are available from Hayrapetyan (2025). At the lower frequency range of the study, the flame tended to only exhibit SOC with increasing pressure excitation amplitude prior to flame blowoff. At a moderate excitation frequency range, the PLOR regime was observed only under specific conditions, likely due to conditions that allowed for the instantaneous Rayleigh index variation described in § 4.2. This behaviour tended to disappear once PFLO occurred, which predominantly took place at higher forcing frequencies. However, clearly, at higher frequency excitation, the flame was able to retain some measure of stabilisation and to avoid flame blowoff, whereas the susceptibility to blowoff was greater at lower frequency excitation. For a given injector, the fuel Reynolds numbers had the ability to scale and shift the flame response along the axes of the frequency and pressure perturbation amplitude of this notional response chart. For the wide parameter range of experiments done, the amplitudes that led to transitions from SOC to PLOR to PFLO and eventually to BO could be extracted from the datasets. Trends may be identified in the key

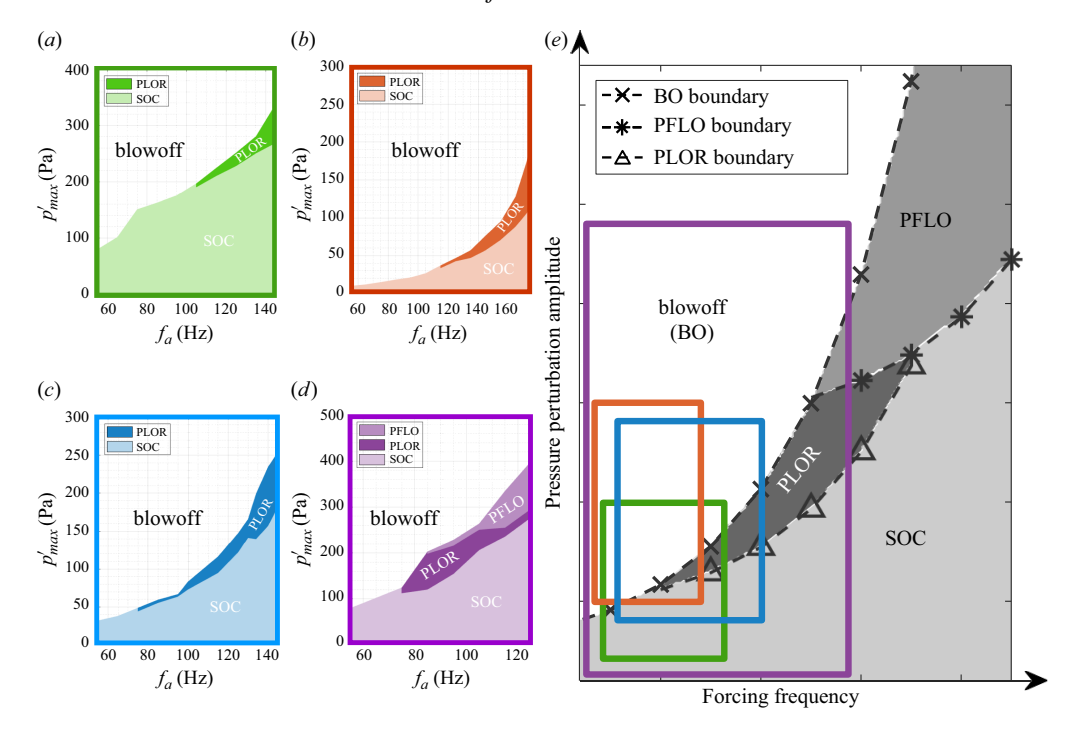


Figure 23. (a-d) Charts representing flame response for four alternative single-jet injectors at different Reynolds numbers for a range of PAN excitation frequencies and amplitudes. (e) Single notional chart for alternative conditions explored, where symbol \triangle represents the transition condition from SOC to PLOR, * represents the transition condition to PFLO and × represents the pressure amplitude causing flame BO. The dashed lines represent the approximate transition boundaries. (a) Small-Thin, Re = 20, (b) Medium-Thin, Re = 11, (c) Medium-Thin, Re = 20, (d) Medium-Thin, Re = 46 and (e) Notional response.

injector design parameters that influence the flame stability and response to the acoustic forcing.

6.1. Effects of jet diameter, Reynolds number and forcing frequency

Figure 24 summarises the transition points for the four different single-jet geometries across various Reynolds numbers, based on local forcing amplitudes and applied frequencies. Overall, higher fuel Reynolds numbers and forcing frequencies were able to accommodate greater pressure perturbation amplitudes to achieve comparable flame liftoff and intensity oscillation, which inevitably led to blowoff. This was also consistent with the turbulent single-jet studies by AFRL (Plascencia *et al.* 2024*a*) and prior UCLA studies involving acoustic forcing for single jets near a pressure node (Vargas *et al.* 2023). The single-jet configurations used in both the AFRL and UCLA studies showed no clear natural instability under unforced conditions, and both exhibited a positive correlation between improved flame stability, i.e. the ability to withstand excitation at higher amplitudes, and forcing frequency. In the present experiments, in the frequency range of 55–165 Hz, the Small-Thin and Small-Thick did not exhibit PFLO under the excitation conditions examined, whereas the Medium-Thin and Large-Thin displayed PFLO at the higher fuel flow rates. Additionally, PLOR was not observed before flame blowoff at the higher flow rates for the Small-Thin and Small-Thick injectors.

Experiments conducted at Reynolds numbers of 20 and 40 for single-jet geometries with varying inner diameters revealed interesting trends in flame response, as summarised

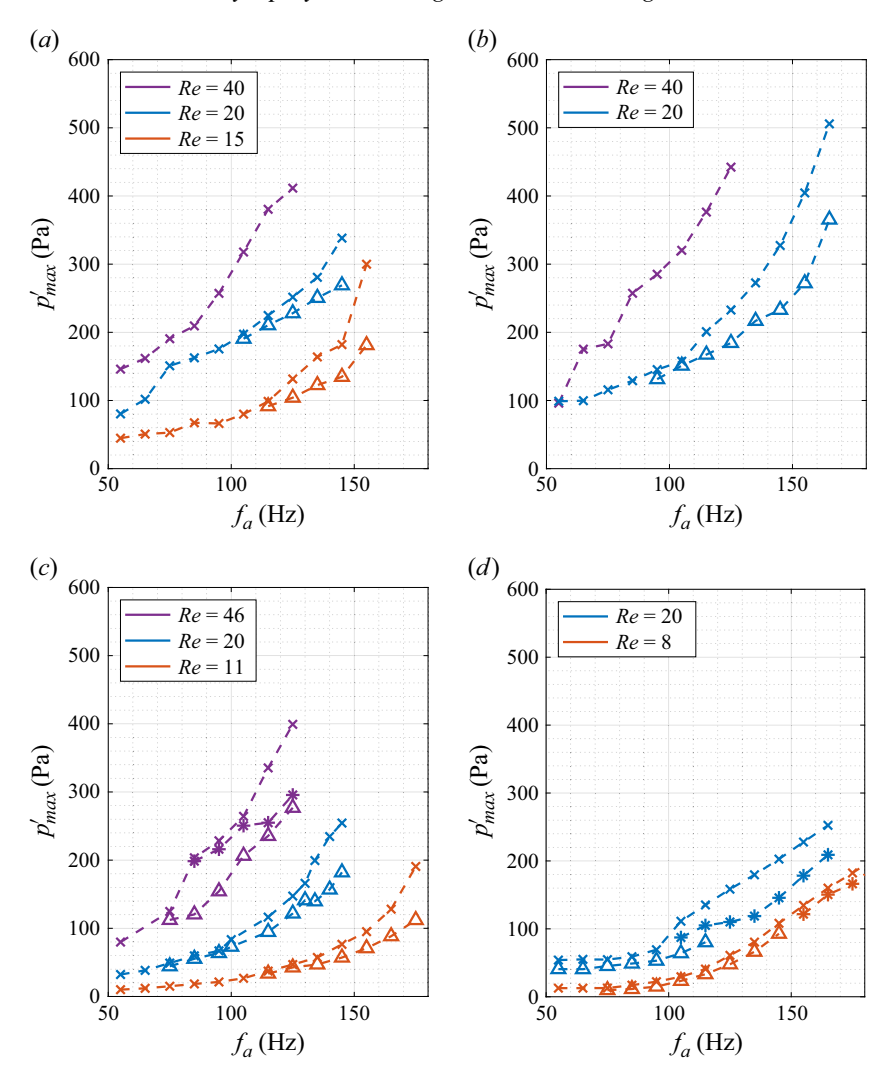


Figure 24. Experimentally determined amplitudes of transition for the different single-jet geometries at various Reynolds numbers, based on local forcing amplitude p'_{max} and applied forcing frequency. The symbol \triangle represents the transition condition from SOC to PLOR, * represents the transition condition to PFLO and \times represents the pressure amplitude causing flame BO. The dashed lines represent the approximate transition boundaries. (a) Small-Thin, (b) Small-Thick, (c) Medium-Thin and (d) Large-Thin injector geometries.

in figure 25. The results indicated that, even at the same Reynolds number, the smaller-diameter jets, with higher bulk velocities, withstood greater pressure perturbation amplitudes prior to blowoff than the other injectors did, despite the significantly lower fuel flow rate, represented in table 2 and figure 3. In contrast, the larger-diameter jets with lower bulk velocities were more susceptible to permanent flame liftoff and blowoff at the same forcing amplitude. The enhanced stability of smaller-diameter jets was possibly due to the higher velocity and momentum flux, which resulted in smaller perturbations in the surrounding gas into which the fuel was injected, as compared with the higher velocity of the incoming fuel. The Medium-Thin jet results shown in figure 25(b), though at a slightly higher fuel flow rate and Reynolds number of Re = 46 as compared with the other cases shown, could not sustain the pressure perturbation amplitudes that could be accommodated

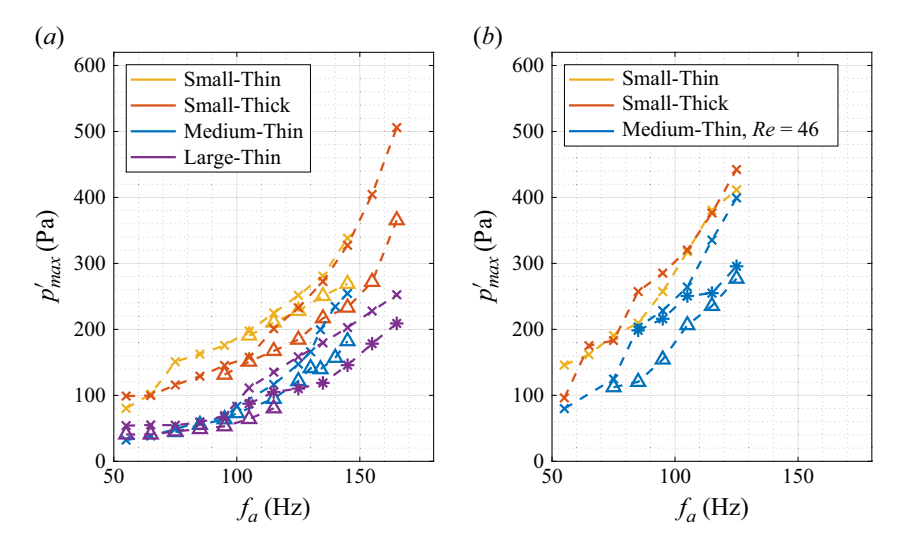


Figure 25. Flame response summary for the different single-jet geometries at Reynolds number of (a) 20 and (b) 40. \triangle represent the transition point from SOC to PLOR, * represent the transition point to PFLO and \times represents the pressure amplitude causing flame BO. The dashed lines represent the approximate transition boundaries respectively.

by the smaller diameter jets. While inner diameter (and thus jet velocity) had a systematic influence on stability at a PAN, the inner tube's wall thickness, however, was found to have a minimal impact on flame stability for single jets. For instance, the Small-Thick injector, which has a wall thickness three times greater than that of the Small-Thin injector, did not exhibit significantly improved flame attachment or stability under the same forcing conditions at either Reynolds number 20 or 40, despite the potential for formation of a recirculation zone adjacent to the thick wall, which could assist in flame stabilisation (Habib & Whitelaw 1979). This idea will be explored further in examining coaxial jet configurations.

6.2. Effects of velocity ratio

The study of coaxial jets focused on the dependence of the forcing frequency and annularto-inner velocity ratio R on blowoff conditions, i.e. withstandable p'_{max} . Figure 26 provides plots of excitation amplitude p'_{max} associated with flame blowoff for the SAR-Thin coaxial jet for a range of velocity ratios R and forcing frequencies, for two different inner jet Reynolds numbers. Unlike the UCLA pressure node study on coaxial fuel jets (Vargas, Hayrapetyan & Karagozian 2025), where an increase in velocity ratio or annular air flow rate was found to shield the flame from transverse velocity perturbations, effectively increasing flame anchoring and stability, the effect of increasing R showed generally an opposite effect for flames exposed to a pressure antinode. This observation was consistent with the AFRL experiments (Plascencia et al. 2024b), which reveal that flow conditions with higher R are more susceptible to transitions from an anchored flame to a permanently lifted flame. Yet the AFRL experiments on coaxial jets exhibit an opposite trend with respect to forcing frequency as compared with the trends in figures 26(a) and 26(b). Plascencia et al. (2024b) reported that at higher frequencies, the flame appears less stable when subject to similar excitation amplitudes in contrast to the increased p'_{max} that can be accommodated at higher forcing frequencies before blowoff in the present experiments. This behaviour may be attributed, in the AFRL experiments, to the increasing excitation

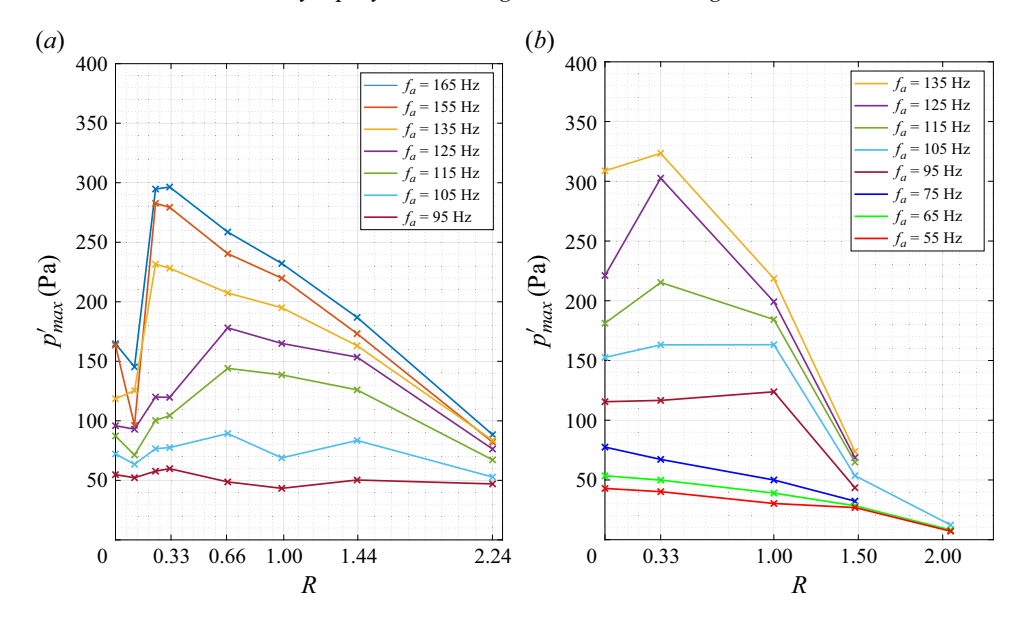


Figure 26. Experimentally determined amplitudes of blowoff for the SAR-Thin coaxial jet at (a) $Re_1 = 10$ and (b) $Re_1 = 20$ at various velocity ratios R, based on local forcing amplitude and applied forcing frequency. The \times markers represent the amplitude causing flame blowoff.

frequency approaching the natural (unforced) frequency of their flame, which is found to be approximately 1500 Hz (Plascencia 2021). As the excitation frequency nears the natural instability frequency, the jet becomes more responsive to perturbations and increasingly able to lock-in to the natural dynamics more easily, requiring much lower amplitudes of excitation (Li & Juniper 2013*a*,*b*). In the present study, however, no natural instability was detected in any of the coaxial jet configurations and, as a result, lock-in could not be achieved. The observed behaviour aligned with the expectation that the flame becomes less responsive at higher excitation frequencies, similar to the single jets, which also did not indicate the presence of natural instabilities in the absence of acoustic excitation.

The results in figure 26 suggest a nonlinear and frequency-dependent influence in the effect of R on flame stability. An optimal R existed where the flame achieved maximum stability; here, a peak blowoff p'_{max} occurred at lower R for higher forcing frequencies and shifted to larger R at lower frequencies. Beyond this optimal condition, as R increased further and the unforced flame became naturally lifted, the flame was more susceptible to blowoff, where blowoff p'_{max} values converged to similar values at the highest velocity ratio R, regardless of frequency. At low frequencies, no clear optimal R was found, and the flame blowoff was at approximately the same or progressively lower pressure amplitudes across the range of R values explored. These trends remained consistent across the different coaxial configurations examined, as will be shown.

6.3. *Effects of area ratio*

The role of the annular-to-inner jet area ratio in influencing blowoff resistance was evaluated across MAR-, LAR- and XLAR-Thick configurations at a fuel Reynolds number of 40, under varying velocity ratios R and forcing frequencies f_a . The p'_{max} boundaries associated with blowoff are summarised in figure 27, where each coaxial jet showed a peak blowoff p'_{max} at different R values, depending on the forcing frequency, similar

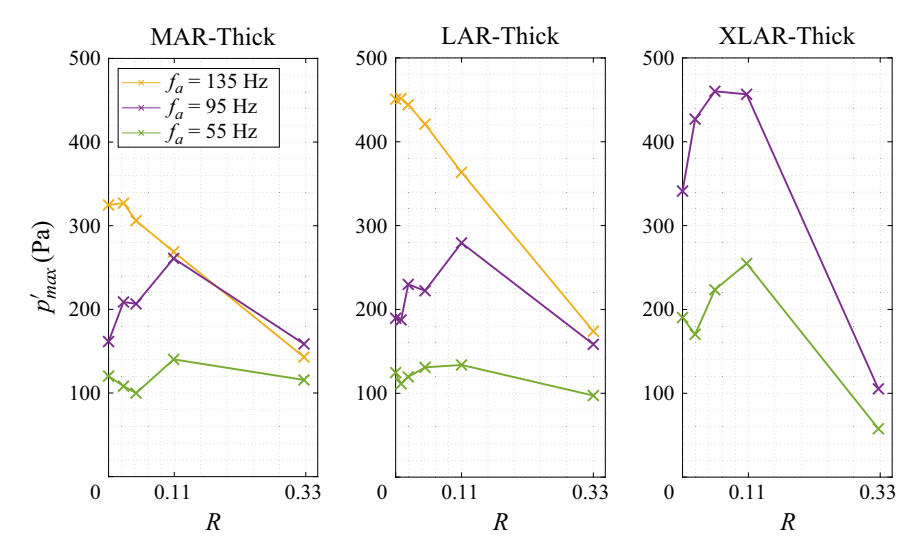


Figure 27. Comparison of the effect of area ratio on coaxial jets at $Re_1 = 40$ at various velocity ratios R, based on local forcing amplitude and applied forcing frequency. The symbol \times represents the amplitude causing flame blowoff.

to observations for the SAR-Thin injector shown in figure 26. The MAR- and LAR-Thick configurations exhibited comparable blowoff trends at 55 and 95 Hz; however, at 135 Hz, the LAR-Thick demonstrated a greater ability to withstand higher p'_{max} before blowoff. For $R \le 0.11$, where the flames in all three configurations remained attached, the XLAR-Thick (with the largest area ratio) withstood the highest p'_{max} . Conversely, at R = 0.33, where natural liftoff occurred in all configurations, the XLAR-Thick withstood the lowest p'_{max} and thus was slightly less stable than the others at higher velocity ratios. This observation may be due to the fact that, despite the matched velocity ratios, the XLAR-Thick exhibited a significantly higher volumetric air flow rate, over double that of the LAR-Thick and more than triple that of the MAR-Thick, resulting in a highly lifted unforced flame which stabilised at approximately $13D_{i,1}$, as seen in figure 5(e). These findings suggested that at lower R, when the flame remains attached, a larger area ratio enhanced flame stability, whereas once natural liftoff occurs, there can be a significant reduction in the withstandable p'_{max} .

6.4. Effects of inner wall thickness

To examine the effect of wall thickness on blowoff resistance, the acoustic responses of the LAR-Thin and LAR-Thick configurations, differing by a threefold increase in inner tube wall thickness, were compared. The corresponding blowoff p'_{max} , summarised in figure 28, indicated the resistance to BO exhibited consistent magnitudes for the thin and thick injectors, though with differing nonlinear dependence on prescribed velocity ratio. At $f_a = 55$ Hz, the BO p'_{max} values were comparable across the two coaxial configurations. At $f_a = 95$ Hz, the R value producing a peak in p'_{max} for the LAR-Thin case was approximately 0.11, whereas for the LAR-Thick case, R producing a peak in p'_{max} was at a higher velocity ratio, approximately 0.33. At 135 Hz, the BO p'_{max} was similar for $R \le 0.11$, but the LAR-Thick exhibited greater resilience at nearly every R value in comparison with the thin injector wall case. The R value at which natural liftoff begins may serve as an indicator of the flame's ability to withstand forcing.

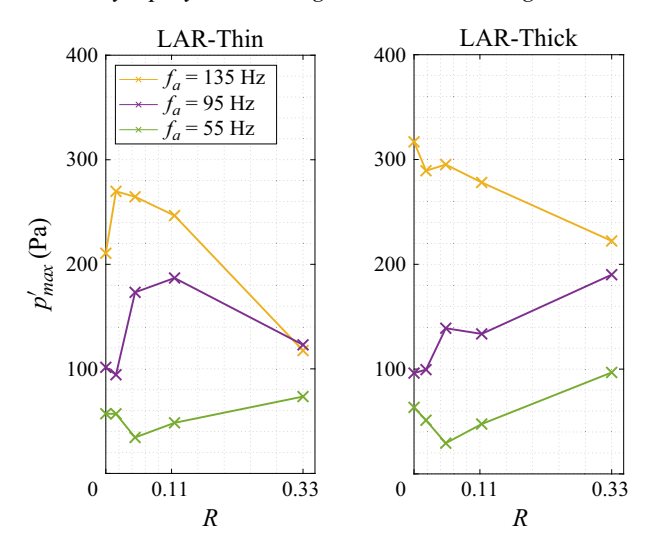


Figure 28. Comparison of the effect of inner wall thickness on coaxial jets at $Re_1 = 20$ at various velocity ratios R, based on local forcing amplitude and applied forcing frequency. The symbol \times represents the amplitude causing flame blowoff.

7. Conclusions

The experimental findings presented in this study offer valuable insights to the dynamics of acoustically coupled combustion systems and how alternative fuel injector geometries can impact flame stability in the presence of acoustic perturbations. In this study, both single and coaxial injectors with various geometrical characteristics (4 and 5 of each type, respectively) were used to create laminar diffusion flames within a closed cylindrical waveguide, emphasising the interaction at a pressure antinode. By systematically varying acoustic forcing frequencies and amplitudes, the effects of key parameters including jet diameter, tube wall thickness, annular-to-inner area and velocity ratio, and jet Reynolds number were explored in relation to flame behaviour and resistance to blowoff. Several flame-acoustic coupling phenomena were identified via visible imaging, including sustained oscillatory combustion (SOC), multi-frequency periodic liftoff and reattachment (PLOR), and permanent flame liftoff (PFLO). Flame blowoff (BO) was documented to occur for a range of conditions for different injector geometries, and while in some cases the flame needed to transition from SOC to PLOR to PFLO before blowing off, in other cases the transition occurred immediately from SOC to BO, or from SOC to PLOR to BO, as shown notionally in figure 23; specific excitation conditions for these transitions are highly dependent on the injector and flow conditions.

This study documented the remarkable range of characteristic signatures associated with such flame transitions and, more importantly, types of injectors and flow conditions that enabled resistance to acoustically driven flame transition and blowoff. Proper orthogonal decomposition (POD)-based mode shapes, phase portraits and spectral characteristics revealed distinct structural and coupling differences among behaviours for SOC, PLOR (with typical subharmonic initiation and an abrupt creation of multiple loops in phase trajectories) and PFLO (with simpler oscillations and phase portraits with more gradual transitions in phase trajectories from SOC). The average phase lag between local pressure perturbations and flame response (either oscillations in visible luminosity or OH* chemiluminescence) was quantified, revealing that transitions to periodic liftoff and reattachment typically occurred when the acoustics and heat release rate were close to

being in-phase, while permanent liftoff was generally observed when they operated more closely to being out-of-phase.

For the single jets, inner jet diameter and hence bulk jet velocity played the more crucial role in improved flame stability at matching Reynolds number, while wall thickness had a less significant impact. In contrast, for the coaxial jets, a larger area ratio with lower air injection velocity as compared with the inner jet velocity enhanced stability at velocity ratios where the flame remained attached. An optimal velocity ratio was identified where maximum flame stability could be achieved, with peak blowoff resistance shifting depending on forcing frequency. Beyond this condition, as the velocity ratio increased further and the unforced flame became naturally lifted, the flame was more susceptible to blowoff, where the blowoff pressure amplitude converged to similar values at the highest velocity ratios, regardless of frequency. These findings underscored the importance of tuning inner and outer iet velocities in coaxial injectors to optimise stability and anchoring, and also to prevent premature liftoff, particularly when constrained by fixed volumetric flow rates. It is noted that many of these observations were consistent with those of Plascencia et al. (2024a,b), e.g. the improved flame stability for the single jets at higher frequency excitation. The fact that the present studies explored nine different injectors, with the ability to study a much wider range of velocity ratios, area ratios and other parameters enabled our trends, though more complicated, to help to define improved injector geometries.

A key takeaway from this study is the importance of quantifying the acoustic characteristics of the injector and combustion chamber, and making use of characteristic signatures from relatively simple diagnostics to determine the state of the unstable behaviour. A priori knowledge or prediction of the state of the combustion instability would help enormously in future engine designs. The fact that the present and recent (Vargas et al. 2023, 2025) dynamical flame characteristics at low Reynolds numbers are very similar to those documented in others' studies of a similar configuration, but at Reynolds numbers two orders of magnitude greater (Plascencia et al. 2024a,b), provides additional evidence for this conclusion.

In general, flame-acoustic coupling is inherently nonlinear, and the present studies demonstrate not only the clear need for reduced order models (ROMs) developed from experimental datasets, and development of ROMs and high-fidelity computational simulations, but also the benefits to industry of understanding and being able to predict dynamical transitions. In this paper, we showed that high-speed spatiotemporal imaging, combined with proper orthogonal decomposition analysis, revealed distinct phase portraits and spectral signatures corresponding to instability transitions. These signatures may provide a foundation for ROM development, a valuable tool for enabling the prediction and control of combustion instabilities. As pressure perturbations increase, mode-coupling trajectories derived from POD analysis exhibit alterations, resulting in asymmetries and alterations in phase portraits during the transition from SOC to PLOR and PFLO. By leveraging data-driven techniques such as Sparse Identification of Nonlinear Dynamics (SINDy) (Brunton, Proctor & Kutz 2016), in fact, recent studies have shown that such acoustic signature-based ROMs can be developed to capture the complex dynamics of acoustically coupled flames (Lettieri et al. 2025). This approach offers a promising pathway for analysing and predicting flame behaviour under varying acoustic conditions, ultimately aiding in the design and optimisation of injector configurations for practical combustion systems.

Supplementary movies. Supplementary movies are available at https://doi.org/10.1017/jfm.2025.10701.

Acknowledgements. The authors wish to acknowledge the assistance of Daniel Oviedo and Qiyuan 'Bill' Wu on this research project.

Funding. This research was funded by the Air Force Office of Scientific Research (AFOSR) under Award Nos. FA9550-19-1-0096 and FA9550-22-1-0190, with Dr. M. Birkan and Dr. Justin Koo as programme managers. The authors thank Kulite Semiconductor Products, Inc. and Elite Motion Systems, LLC (President L. Vladic) for donating pressure transducers and the lens used in this study, respectively, and to Mr. F. Stanback for his donation of funds enabling the purchase of the high-speed camera.

Declaration of interests. The authors report no conflict of interest.

REFERENCES

- BAILLOT, F. & DEMARE, D. 2002 Physical mechanisms of a lifted nonpremixed flame stabilized in an acoustic field. *Combust. Sci. Technol.* **174** (8), 73–98.
- BAILLOT, F. & DEMARE, D. 2007 Responses of a lifted non-premixed flame to acoustic forcing. part 2. *Combust. Sci. Technol.* **179** (5), 905–932.
- BENNEWITZ, J.W., VALENTINI, D., PLASCENCIA, M.A., VARGAS, A., SIM, H.S., LOPEZ, B., SMITH, O.I. & KARAGOZIAN, A.R. 2018 Periodic partial extinction in acoustically coupled fuel droplet combustion. *Combust. Flame* 189, 46–61.
- BROUZET, D., YOU, S., PLASCENCIA, M.A., ROA, M. & IHME, M. 2022 The dynamics of non-premixed flames subjected to a transverse acoustic mode. *Combust. Flame* **246**, 112330.
- BRUNTON, S.L., PROCTOR, J.L. & KUTZ, J.N. 2016 Discovering governing equations from data by sparse identification of nonlinear dynamical systems. *Proc. Natl Acad. Sci.* 113 (15), 3932–3937.
- CANDEL, S.M. 1992 Combustion instabilities coupled by pressure waves and their active control. *Symp. (Intl) Combust.* **24** (1), 1277–1296. Twenty-Fourth Symposium on Combustion.
- CHEN, L.-W., WANG, Q. & ZHANG, Y. 2012 Flow characterisation of diffusion flame in a standing wave. Exp. Therm. Fluid Sci. 41, 84–93.
- CHEN, S., ZHAO, D., LI, H.K.H., NG, T.Y. & JIN, X. 2017 Numerical study of dynamic response of a jet diffusion flame to standing waves in a longitudinal tube. *Appl. Therm. Engng.* **112**, 1070–1082.
- CHUNG, S.H. & LEE, B.J. 1991 On the characteristics of laminar lifted flames in a nonpremixed jet. *Combust. Flame* **86** (1–2), 62–72.
- CHUNG, S.H. & LEE, B.J. 1997 Stabilization of lifted tribrachial flames in a laminar nonpremixed jet. *Combust. Flame* **109** (1–2), 163–172.
- CROCCO, L. & CHENG, S.-I. 1956 Theory of combustion instability in liquid propellant rocket motors.
- CULICK, F.E.C. & KUENTZMANN, PAUL 2006 Unsteady motions in combustion chambers for propulsion systems, NATO RTO-AG-AVT-039AGARDograph.
- FEIKEMA, D., CHEN, R.-H. & DRISCOLL, J.F. 1991 Blowout of nonpremixed flames: maximum coaxial air velocities achievable, with and without swirl. *Combust. Flame* **86** (4), 347–358.
- FORLITI, D.J., LEYVA, I.A., TALLEY, D.G., RODRIGUEZ, J.I., TESHOME, S., WEGENER, J.L., ROA, M. & KARAGOZIAN, A.R. 2020 Forced and unforced shear coaxial mixing and combustion at subcritical and supercritical pressures. In *Chapter 6 in High Pressure Flows for Propulsion Applications, AIAA Progress in Astronautics and Aeronautics*, pp. 233–279.
- GAO, J., HOSSAIN, A., MATSUOKA, T. & NAKAMURA, Y. 2017 A numerical study on heat-recirculation assisted combustion for small scale jet diffusion flames at near-extinction condition. *Combust. Flame* 178, 182–194.
- HABIB, M.A. & WHITELAW, J.H. 1979 Velocity characteristics of a confined coaxial jet. *J. Fluids Engng.* **101** (4), 521–529.
- HARRJE, D.T. 1972 Liquid propellant rocket combustion instability. *NASA Special Publication Rep.* No. NASA-SP-194. NASA Headquarters, Washington, DC.
- HAYRAPETYAN, ARIN 2025 Acoustically coupled gaseous combustion dynamics, PhD dissertation. University of California, Los Angeles.
- HAYRAPETYAN, A., VARGAS, A. & KARAGOZIAN, A.R. 2025 Denoising neural network for low-light imaging of acoustically coupled combustion. *Exp. Fluids* **66**, 59.
- LETTIERI, D., VARGAS, A., KARAGOZIAN, A.R. & ALVES, L. 2025 Sparse identification of nonlinear dynamics from under-sampled periodic datasets. In *To appear in Proceedings of the Royal Society A*.
- LI, L.K.B. & JUNIPER, M.P. 2013a Lock-in and quasiperiodicity in hydrodynamically self-excited flames: Experiments and modelling. *Proc. Combust. Inst.* **34** (1), 947–954.
- LI, L.K.B. & JUNIPER, M.P. 2013b Lock-in and quasiperiodicity in a forced hydrodynamically self-excited jet. J. Fluid Mech. 726, 624–655.
- LIEUWEN, T., TORRES, H., JOHNSON, C. & ZINN, B.T. 2001 A mechanism of combustion instability in lean premixed gas turbine combustors. *J. Engng Gas Turb. Power* 123 (1), 182–189.

- LINAN, A., VERA, M. & SANCHEZ, A.L. 2015 Ignition, liftoff, and extinction of gaseous diffusion flames. *Annu. Rev. Fluid Mech.* **47** (1), 293–314.
- MAGINA, N., ACHARYA, V. & LIEUWEN, T. 2019 Forced response of laminar non-premixed jet flames. Prog. Energy Combust. Sci. 70, 89–118.
- PLASCENCIA, M.A. 2021 Combustion dynamics of liquid droplets and turbulent jets relevant to rocket engines, PhD dissertation. University of California, Los Angeles.
- PLASCENCIA, M.A., TALLEY, D.G., ROA, M., KARAGOZIAN, A.R. & MUNIPALLI, R. 2024a Lifting of single and coaxial nonpremixed jet flames under transverse acoustic forcing. AIAA J. 62 (1), 140–152.
- PLASCENCIA, M.A., TALLEY, D.G., ROA, M., KARAGOZIAN, A.R. & MUNIPALLI, R. 2024b Lifting of transversely forced turbulent nonpremixed coaxial jet flames. AIAA J. 62 (9), 3294–3304.
- RAYLEIGH, L. 1896 The Theory of Sound, vol. 2. Macmillan.
- SEVILLA-ESPARZA, C.I., WEGENER, J.L., TESHOME, S., RODRIGUEZ, J.I., SMITH, O.I. & KARAGOZIAN, A.R. 2014 Droplet combustion in the presence of acoustic excitation. *Combust. Flame* **161** (6), 1604–1619.
- SIM, H.S., PLASCENCIA, M.A., VARGAS, A., BENNEWITZ, J.W., SMITH, O.I. & KARAGOZIAN, A.R. 2019 Effects of inert and energetic nanoparticles on burning liquid ethanol droplets. *Combust. Sci. Technol.* 191 (7), 1079–1100.
- SIM, H.S., PLASCENCIA, M.A., VARGAS, A. & KARAGOZIAN, A.R. 2020a Acoustically forced droplet combustion of liquid fuel with reactive aluminum nanoparticulates. *Combust. Sci. Technol.* 192 (5), 761–785.
- SIM, H.S., VARGAS, A., AHN, D.D. & KARAGOZIAN, A.R. 2020b Laminar microjet diffusion flame response to transverse acoustic excitation. *Combust. Sci. Technol.* **192** (7), 1292–1319.
- TANABE, M., KUWAHARA, T., SATOH, K., FUJIMORI, T., SATO, J. & KONO, M. 2005 Droplet combustion in standing sound waves. *Proc. Combust. Inst.* **30** (2), 1957–1964.
- TANABE, M., MORITA, T., AOKI, K., SATOH, K., FUJIMORI, T. & SATO, J. 2000 Influence of standing sound waves on droplet combustion. *Proc. Combust. Inst.* 28 (1), 1007–1013.
- VARGAS, A. 2022 Acoustically coupled, non-premixed combustion processes, PhD dissertation. University of California, Los Angeles.
- VARGAS, A., HAYRAPETYAN, A. & KARAGOZIAN, A.R. 2025 Dynamics of acoustically excited coaxial laminar jet diffusion flames. *Combust. Flame* **274**, 114029.
- VARGAS, A., KIANI, S., HAYRAPETYAN, A. & KARAGOZIAN, A.R. 2023 Dynamics of acoustically coupled single- and multi-port jet diffusion flames. *J. Fluid Mech.* 972, A21.
- WILLIAMS, T.C., SHADDIX, C.R., SCHEFER, R.W. & DESGROUX, P. 2007 The response of buoyant laminar diffusion flames to low-frequency forcing. *Combust. Flame* 151 (4), 676–684.
- WON, S.H., CHUNG, S.H., CHA, M.S. & LEE, B.J. 2000 Lifted flame stabilization in developing and developed regions of coflow jets for highly diluted propane. *Proc. Combust. Inst.* 28 (2), 2093–2099.